

GRAPH THEORY FOR ANALYZING PAIR-WISE DATA:
APPLICATION TO INTERFEROMETRIC SYNTHETIC
APERTURE RADAR DATA

by

Elena C. Reinisch

A thesis submitted in partial fulfillment of
the requirements for the degree of

Master of Science

(Geophysics)

at the

UNIVERSITY OF WISCONSIN-MADISON

2016

Date of final oral examination: 05/19/2016

This thesis is approved by the following members of the Final Oral Committee:

Kurt L. Feigl, Professor, Geoscience

Michael Cardiff, Assistant Professor, Geoscience

Clifford H. Thurber, Vilas Distinguished Professor, Geoscience

Abstract

Graph theory is useful for estimating time-dependent model parameters via weighted least-squares using interferometric synthetic aperture radar (InSAR) data. Plotting acquisition dates (epochs) as vertices and pair-wise interferometric combinations as edges defines an incidence graph. The edge-vertex incidence matrix and the normalized edge Laplacian matrix are factors in the covariance matrix for the pair-wise data. Using empirical measures of residual scatter in the pair-wise observations, we estimate the variance at each epoch by inverting the covariance of the pair-wise data. We evaluate the rank deficiency of the corresponding least-squares problem via the edge-vertex incidence matrix. We implement our method in a MATLAB software package called GraphTreeTA available on GitHub (<https://github.com/feigl/gipht>). We apply temporal adjustment to the data set described in Lu et al. (2005) at Okmok volcano, Alaska, which erupted most recently in 1997 and 2008. The data set contains 44 differential volumetric changes and uncertainties estimated from interferograms between 1997 and 2004. Estimates show that approximately half of the magma volume lost during the 1997 eruption was recovered by the summer of 2003. Between June 2002 and September 2003, the estimated rate of volumetric increase is $(6.2 \pm 0.6) \times 10^6 \text{ m}^3/\text{yr}$. Our preferred model provides a reasonable fit that is compatible with viscoelastic relaxation in the five years following the 1997 eruption. Although we demonstrate the approach using volumetric rates of change, our formulation in terms of incidence graphs applies to any quantity derived from pair-wise differences, such as wrapped phase or wrapped residuals.

Acknowledgements

We thank Piyush S. Agram and Mark Simons for providing results in advance of publication, as well as H el ene Le M evel, S. Tabrez Ali, and Cliff Thurber for helpful discussions. Additionally, we thank Zhong Lu, Summer Ohlendorf, and Jeff Freymueller for sharing their results on Okmok. The data used in this paper have been published by Lu et al. (2005).

I would like to personally thank my research advisor, Kurt L. Feigl and my committee members Michael Cardiff and Clifford Thurber for their wisdom and guidance. In addition, I would like to thank Rebecca Willett for her mentorship. I would also like to thank my fellow research group members H el ene Le M evel and S. Tabrez Ali, for being excellent role models and my husband Alex Reinisch, for his continued support.

This material is based upon work supported by the National Science Foundation Graduate Research Fellowship under Grant No. DGE-1256259, the National Aeronautics and Space Administration under grant NNX12AO37G, and by the National Science Foundation under grants EAR-0943965 and EAR-1347190.

This manuscript (except Section 6) has been submitted to the *Journal of Geodesy* with the title “Graph theory for analyzing pair-wise data: Application to geophysical model parameters estimated from interferometric synthetic aperture radar data at Okmok Volcano, Alaska” by Elena C. Reinisch, Michael Cardiff, and Kurt L. Feigl on 2 May 2016.

Contents

1	Introduction	1
1.1	Background of InSAR	1
1.2	Previous Work	2
2	Review of Graph Theory	7
2.1	Relationship Between Components and Undetermined Parameters	7
3	Methods	11
3.1	Example Case: Building the Design Matrix \mathbf{G}	11
3.2	Alternative Parameterization	15
3.3	Design Matrix \mathbf{G} for Other Functions of Time	19
3.4	Defining the Data Covariance Matrix	20
3.5	Example Case: Data Covariance Matrix	22
3.6	Epoch-wise Covariance	23
3.7	Least-Squares Solution Using the Pseudoinverse and Normal Equations	28
3.8	Applying the Forward Model	29
4	Implementation	31
4.1	Description of Functions	31
5	Application to Okmok Volcano	33
5.1	Background of Okmok Volcano	33
5.2	Setting up the Inverse Problem	37
5.3	Estimation of Epoch-wise Variance	40
5.4	Single-segment Secular Rate Parameterization	42
5.5	Five-segment Piecewise-linear Parameterization	44
5.6	Berardino Parameterization	46

5.7	Exponential Decay Parameterization	49
5.8	Modified Exponential Parameterization	50
6	Discussion	55
6.1	Estimating the Characteristic Time Scale at at Okmok Volcano	55
6.2	Viscoelastic Relaxation of the Surrounding Country Rock	58
6.3	Viscous Magma Flow Upwards Through a Conduit	60
6.4	Secondary Pulses?	67
7	Conclusions	69
	Appendix A Mathematical Notation	71
	Appendix B Revised Data Table from Lu et al. (2005)	75
	Bibliography	79

1 Introduction

1.1 Background of InSAR

Interferometric synthetic aperture radar (InSAR) measures the deformation of an area on the ground by calculating the difference in phase between two synthetic aperture radar (SAR) images covering the same location taken at two different points in time (“epochs”) (e.g., Massonnet and Feigl, 1998). Like many geodetic techniques, including spirit leveling, triangulation by theodolite, trilateration by electronic distance measurement (EDM), and very long baseline interferometry (VLBI), InSAR makes relative measurements as pair-wise differences (e.g., Feigl et al., 2002). Each pixel in an unwrapped interferogram is the difference between the satellite-to-ground range measured at one epoch and the range measured at a second epoch (e.g., Massonnet and Feigl, 1998).

Using the notation conventionally employed in geophysics, we write a linear model as $\mathbf{G}\mathbf{m} = \mathbf{d}$, where \mathbf{d} is a vector containing n pair-wise measurements, \mathbf{m} is a vector containing m parameters in the geophysical model, and \mathbf{G} is an n -by- m design matrix (e.g., Aster et al., 2013). In the case of pair-wise data, the design matrix \mathbf{G} is an incidence matrix consisting of elements from the set $\{-1, 0, 1\}$ (Strang and Borre, 1997). Alternatively, Schmidt (1996) expresses differences in range in terms of bivectors, or vectors whose elements depend on two different sets of data, to estimate relative position coordinates. To estimate the optimal set of parameters, one conventionally solves the (weighted) least-squares problem. If the geophysical model is a function of time, we call the estimation procedure “temporal adjustment” (Beauducel et al., 2000; Feigl et al., 2002; Berardino et al., 2002; Schmidt and Bürgmann, 2003).

In the case of InSAR, the input data can consist of: (1) a set of differential changes in range along the line of sight at a single pixel, or (2) a set of model parameters estimated from individual interferometric pairs spanning different intervals of time. In the example application that we consider below, the model parameters measure the volumetric change

in a magma chamber below the volcanic edifice. With such data, the number of epochs q is necessarily greater than the minimum number of pair-wise combinations $c = q - 1$ required to span the epochs (Feigl and Thurber, 2009). Consequently, if the number of model parameters m equals the number of epochs q , then the corresponding least-squares problem is necessarily underdetermined. In this case, the design matrix \mathbf{G} is rank-deficient.

For example, suppose we have InSAR data acquired by a radar sensor measuring an inflating volcano. In this case, one pair-wise observation will measure the change in range (distance along the line of “sight” from the sensor to the ground) between the first and second epochs. A decrease in range equals the sensor-ward displacement along the line of sight of the sensor (i.e. the temporal change in a single component of relative position). Without additional constraining information, such as the initial position with respect to a known reference point, we cannot estimate absolute parameters. To solve the least-squares problem, we must reduce the number of parameters and/or add regularizing constraints.

In this paper, we apply graph theory to: (1) visualize model parameters estimated from an InSAR data set, (2) construct the covariance matrix for pair-wise data, (3) estimate the error variance of the measurements at each epoch, (4) evaluate the rank deficiency of the least-squares inverse problem, (5) select appropriate parameterizations of the time-dependent model, and (6) select regularizing constraints.

We have included a table describing our mathematical notation in Appendix A.

1.2 Previous Work

To distinguish between geophysical signals on the ground, perturbations in the atmosphere, and artifacts in the processing, one can compare different interferometric pairs that span different time intervals, as sketched in panels a through c of Figure 1.1 (e.g.,

Massonnet and Feigl, 1995). In terms of graph theory, Figure 1.1 (a) and Figure 1.1 (c) are examples of a tree graph, where the edges of the graph connect the vertices without any cycles. Figure 1.1 (b) is an example of a collection of trees, also known as a forest (Harris et al., 2008).

Biggs et al. (2007) introduce the notion of “chains,” as sketched in Figure 1.1 (d). Constructing a chain of pairs where the second epoch of one pair is the first epoch of the next pair cancels all of the atmospheric contributions except those of the first and last epochs in the chain. In terms of graph theory, a “chain” is a path graph, or a tree with no branches connecting all vertices, such that it has internal nodes of degree two referring to two edge connections and terminal nodes of degree one referring to one edge connection (see Figure 1.1 (d) (e.g., Harris et al., 2008, pg. 6)).

Alternatively, the single-master approach refers all the pairs to a single epoch in a graph that resembles a star (Figure 1.1 (e))(e.g., Hooper et al., 2004; Hooper, 2008). Perissin and Wang (2012) draw the graph of a minimum spanning tree (Figure 1.1 (f)) in two dimensions: time and orbital separation. A minimum spanning tree is a tree that contains all vertices of a graph and has the lowest cost as calculated according to the weight of each edge (e.g., Harris et al., 2008, pg. 39).

Alternatively, one can choose a set of pairs such that the time intervals between successive epochs and the orbital separations (“baselines”) between pairs are as short as possible in an approach known as Small Baseline Subset (SBAS) (Berardino et al., 2002; Lanari et al., 2007; Casu et al., 2008; Lee et al., 2012).

In a different approach, Hetland et al. (2012) generalize the temporal parameterization to include a library of temporal functions in their Multiscale InSAR Time Series (MInTS) procedure. More recently, Agram and Simons (2015) have developed a model for spatial and temporal covariance for interferometric phase noise for use in time-series analysis.

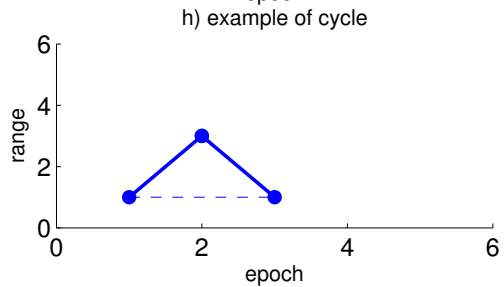
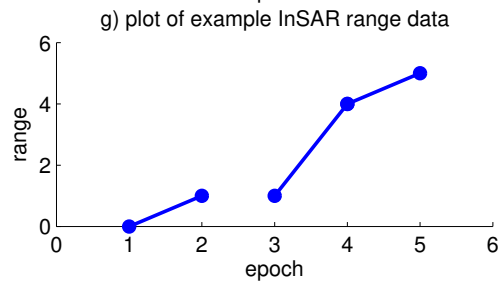
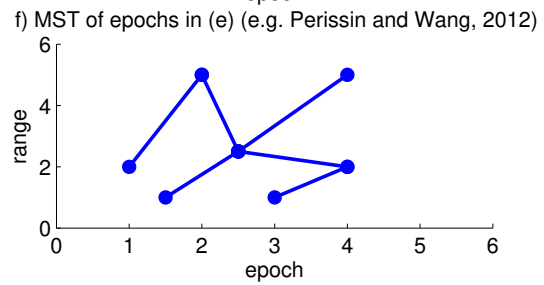
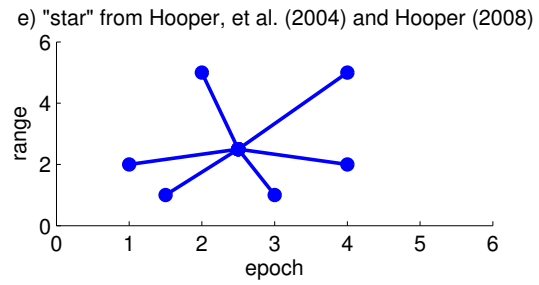
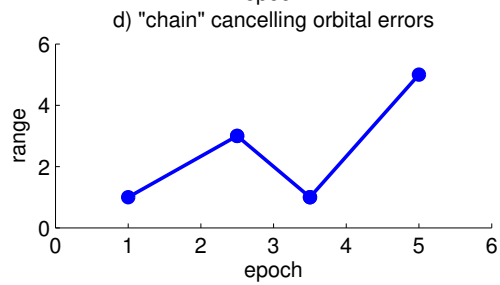
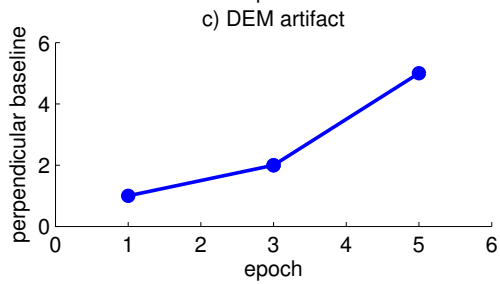
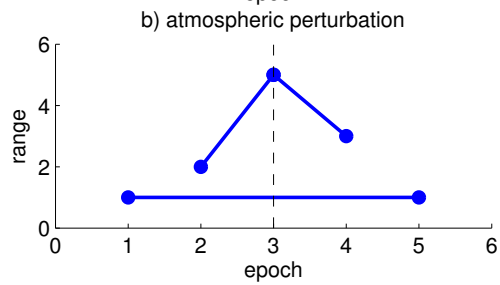
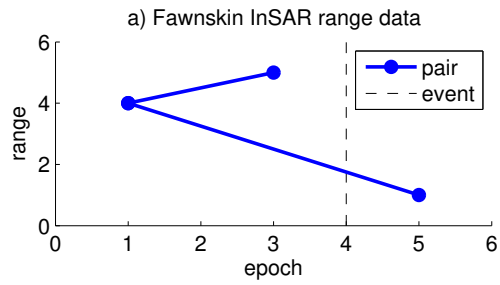


Figure 1.1: Examples of common graphs in InSAR analysis. In each graph, the dots correspond to epochs (vertices) and segments correspond to pairs (edges). (a) Range changes depend on whether or not the measured interval of time spans an event such as the Fawnskin earthquake (Feigl et al., 1995; Feigl and Thurber, 2009). (b) Atmospheric perturbation. The atmospheric perturbation at epoch 3 creates a significant disturbance in pairs (2,3) and (3,4) but not (1,5). (c) An error in the digital elevation model (DEM) can create an artifact in the interferogram such that the range change is proportional to the orbital separation (Massonnet and Feigl, 1995), also known as the “baseline distance B” (Zebker and Goldstein, 1986). (d) A graph of a “chain,” where the chronologically first epoch of one pair is the chronologically second epoch of the previous pair (Biggs et al., 2007). The orbital errors associated with the interior epochs in the chain cancel each other. (e) The graph of a data set that forms a “star” such that each of the second epochs per pair forms a pair with the single master epoch located at the center (Perissin and Wang, 2012). (f) Example of the minimum spanning tree (MST) of the same data set as in Figure 1.1 (e). (g) Incidence graph of example data set containing 5 epochs, 3 pairs, and 2 distinct trees. (h) Three epochs form only two independent pairs (solid line segments). Adding a third pair (dashed line segment) forms a cycle in the graph but adds no additional information to the inverse problem. The information gained from the combination of pairs (1,2) and (2,3) is the same as the information given from pair (1,3).

2 Review of Graph Theory

A graph represents the relationships between a set containing vertices and a set of edges (Harris et al., 2008). When applied to InSAR, the m vertices signify *points* in time, or epochs, and the edges signify the n pair-wise combinations of images, or interferograms that span *intervals* of time. Following the notation of Merris (1994), we draw a directed graph by assigning a direction to each edge, with one end of the pair assigned as the “positive” vertex and the other as the “negative” vertex. For example, given a vertex v_j at an epoch t_j and another vertex v_k at a second, chronologically later, epoch t_k , we denote the i^{th} pair as edge $e_i = \{v_j, v_k\}$. We define an edge-vertex incidence matrix \mathbf{Q} having n rows and m columns first. The i^{th} row at \mathbf{Q} represents the i^{th} pair such that $Q_{i,j} = -1$, $Q_{i,k} = 1$, and $Q_{i,v \notin \{j,k\}} = 0$ for all other vertices other than v_j and v_k . Note that our edge-vertex incidence matrix \mathbf{Q} is the transpose of the m -by- n vertex-edge incidence matrix used by Merris (1994). We use the edge-vertex form of the incidence matrix \mathbf{Q} to lighten the notation.

2.1 Relationship Between Components and Undetermined Parameters

We consider a situation in which InSAR data corresponding to range changes $\Delta\rho$ from a set of n interferometric pairs are derived from SAR images acquired at m epochs. The corresponding system of linear equations is $\mathbf{Q}\mathbf{m} = \mathbf{d}_{obs}$, where $\mathbf{d}_{obs} = \Delta\rho$ is the vector of pair-wise observations and $\mathbf{m} = \boldsymbol{\rho}$ is the vector of m unknown parameters, each of which represents the absolute range from sensor to target at an epoch in time. The solution is underdetermined because the number of unknown parameters m is greater than the number of independent equations $rank(\mathbf{Q})$. The rank deficiency is

$$\mu = m - rank(\mathbf{Q}) \quad (2.1)$$

as demonstrated by Strang and Borre (1997, p. 114, 118).

In some cases, the graph is disconnected, or composed of more than one distinct component (also referred to as a connected component (e.g., Harris et al., 2008, p. 8)). Feigl and Thurber (2009) called each component a “species.” A distinct component in an InSAR data set is a set of individual images that combine pair-wise to form a set of interferograms. The epoch of each image corresponds to a vertex in the graph. Each vertex in a component is connected to at least one other vertex in the component by an edge. One distinct component is not connected to another distinct component. For example, SAR images acquired by one radar sensor are not interferometrically compatible with those from another sensor. The vertices in the corresponding graph thus form two distinct, disconnected components, as sketched in Figure 1.1 (g).

Graph theory tells us that the rank of the incidence matrix for a disconnected graph is

$$\text{rank}(\mathbf{Q}) = m - k \quad (2.2)$$

where m , the number of nodes (or vertices), represents the number of epochs and k is the number of components (Deo, 2004, p. 140). If the components do not contain any cycles, then k also represents the number of distinct trees.

Thus, we can prove that the number of components in a disconnected graph is equal to the rank deficiency of the corresponding incidence matrix.

Theorem 1.

$$k = m - \text{rank}(\mathbf{Q}) = \mu \quad (2.3)$$

Proof. We begin by rewriting equation (2.2) in terms of k :

$$k = m - \text{rank}(\mathbf{Q}) \quad (2.4)$$

We can now see that equation (2.4) is equivalent to our previous definition of rank deficiency as stated in equation (2.1): $\mu = m - \text{rank}(\mathbf{Q})$. Thus,

$$k = m - \text{rank}(\mathbf{Q}) = \mu \tag{2.5}$$

This theorem was noted, but not proven, by Feigl and Thurber (2009).

3 Methods

3.1 Example Case: Building the Design Matrix \mathbf{G}

Let us assume a simple, specific case, as graphed in Figure 1.1 (g), with five epochs $\{v_1, v_2, v_3, v_4, v_5\}$ and three pairs $\{e_{1,2}, e_{3,4}, e_{4,5}\}$. The corresponding graph is disconnected (Figure 1.1 (g)). It includes two distinct components. The first component includes 1 pair and 2 epochs. The second component includes 2 pairs and 3 epochs. Since there are no cycles, each of these two components is a tree. Since the epochs are arranged in chronological order, the graph is directed. Thus, it is a directed acyclic graph (DAG).

The corresponding edge-vertex incidence matrix \mathbf{Q} is:

$$\mathbf{Q} = \begin{bmatrix} -1 & 1 & 0 & 0 & 0 \\ 0 & 0 & -1 & 1 & 0 \\ 0 & 0 & 0 & -1 & 1 \end{bmatrix} \quad (3.1)$$

The system of equations is thus

$$\begin{bmatrix} -1 & 1 & 0 & 0 & 0 \\ 0 & 0 & -1 & 1 & 0 \\ 0 & 0 & 0 & -1 & 1 \end{bmatrix} \begin{bmatrix} m_1 \\ m_2 \\ m_3 \\ m_4 \\ m_5 \end{bmatrix} = \begin{bmatrix} d_{1,2} \\ d_{3,4} \\ d_{4,5} \end{bmatrix} \quad (3.2)$$

$$= \begin{bmatrix} \rho_2 - \rho_1 \\ \rho_4 - \rho_3 \\ \rho_5 - \rho_4 \end{bmatrix}$$

where $\rho_i = \rho(t_i)$ is the range at epoch t_i . Using Figure 1.1 (g), Theorem 1, and equation (2.3), we see that since $\mu = k = 2$, two parameters remain indistinguishable. Thus,

we need to add two constraints to the system in order to regularize the problem. We append two constraining rows to \mathbf{Q} to formulate the design matrix \mathbf{G} for the constrained system $\mathbf{G}\mathbf{m} = \mathbf{d}$. From Figure 1.1 (g), we see that the two initial vertices of interest are v_1 and v_3 , corresponding to epochs t_1 and t_3 .

For simplicity, let us (arbitrarily) constrain the system such that the absolute range at the first epoch in each distinct component is fixed at zero.

$$\begin{aligned}\rho(t_1) = m_1 &= 0 \\ \rho(t_3) = m_3 &= 0\end{aligned}\tag{3.3}$$

From these equations, we define a 2-row constraint matrix \mathbf{C} :

$$\mathbf{C} = \begin{bmatrix} 1 & 0 & 0 & 0 & 0 \\ 0 & 0 & 1 & 0 & 0 \end{bmatrix}\tag{3.4}$$

and a 2-row data constraint vector: $\mathbf{d}_{con} = [0, 0]^T$.

Here, the number of rows in each of \mathbf{C} and \mathbf{d}_{con} is equal to the number of constraints $k = 2$. We construct the design matrix \mathbf{G} from the incidence matrix \mathbf{Q} and the constraint matrix \mathbf{C} :

$$\mathbf{G} = \begin{bmatrix} \mathbf{Q} \\ \mathbf{C} \end{bmatrix}\tag{3.5}$$

For this case,

$$\mathbf{G} = \begin{bmatrix} -1 & 1 & 0 & 0 & 0 \\ 0 & 0 & -1 & 1 & 0 \\ 0 & 0 & 0 & -1 & 1 \\ 1 & 0 & 0 & 0 & 0 \\ 0 & 0 & 1 & 0 & 0 \end{bmatrix}\tag{3.6}$$

We expand the data vector by including the constraining elements of equation (3.3)

in the data vector \mathbf{d} .

$$\mathbf{d} = \begin{bmatrix} \mathbf{d}_{obs} \\ \mathbf{d}_{con} \end{bmatrix} \quad (3.7)$$

Now the system takes the form

$$\begin{bmatrix} \mathbf{Q} \\ \mathbf{C} \end{bmatrix} \begin{bmatrix} \mathbf{m} \end{bmatrix} = \begin{bmatrix} \mathbf{d}_{obs} \\ \mathbf{d}_{con} \end{bmatrix} \quad (3.8)$$

Let us further define a simple data set of range changes $\mathbf{d}_{obs} = [1, 2, 1]^T$ (mm) and a set of epochs at 1-year intervals, $\mathbf{t} = [1, 2, 3, 4, 5]^T$ (yr). Figure 3.1 (a) shows the data set as rates. Figure 3.1 (b) shows how adding constraints leads to a solution.

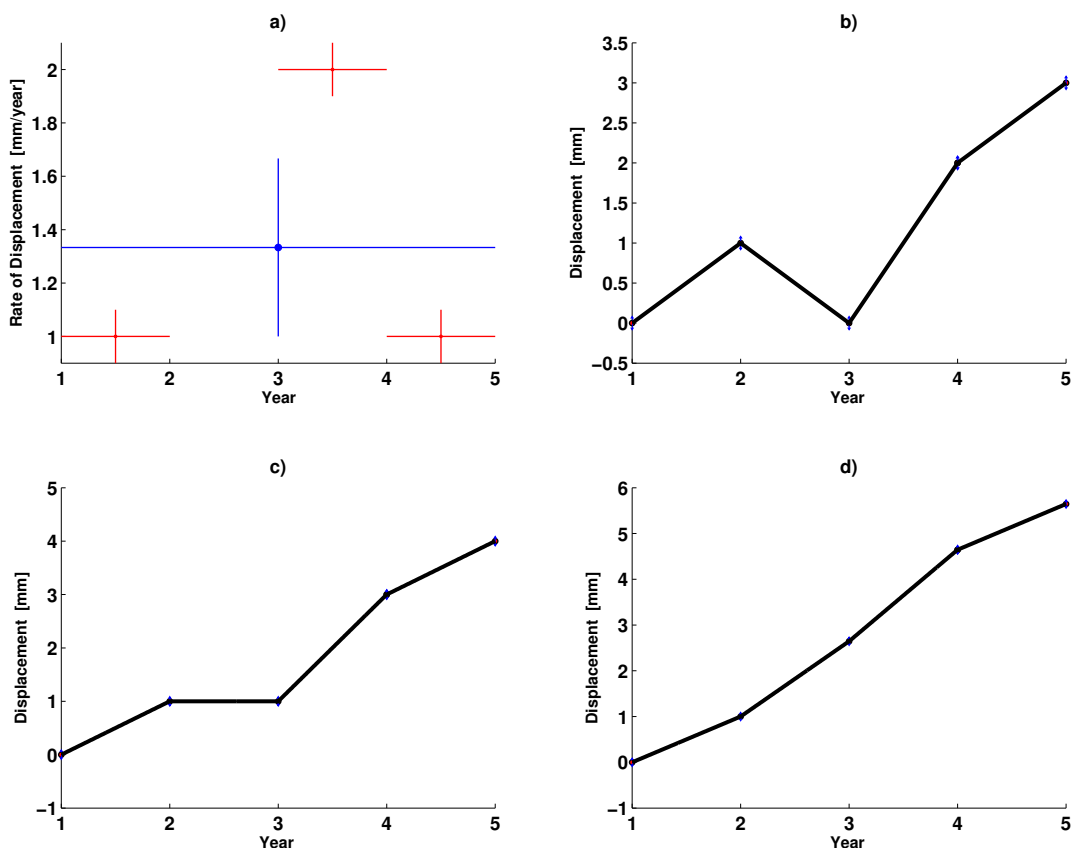


Figure 3.1: Plots illustrating the simple, fictitious example of vertical displacement in an inflating volcano as measured by an InSAR data set with 5 epochs and 3 independent pairs that graph as two distinct trees. (a) Plot of displacement rates for individual pairs with corresponding time intervals (horizontal red bars), and standard deviations of measurement errors (vertical red bars). The blue symbol indicates weighted mean with scaled 68 percent confidence interval (vertical blue bar) and time span for the entire data set (horizontal blue bar). (b) Plot of displacement as a function of time as calculated by temporal adjustment using a piecewise linear parameterization and two constraints. The constraining equations plot as relative displacement within each tree, setting the initial displacement at the first epoch in each distinct component at zero. (c) Plot of displacement as a function of time estimated with a piecewise linear parameterization in terms of velocity using the method outlined in Berardino et al. (2002). (d) Plot of displacement as a function of time estimated using the parameterization in (c) with first-order Tikhonov regularization (penalizing towards a constant-rate solution). The regularization parameter $\beta = 0.0090$.

3.2 Alternative Parameterization

An alternative parameterization is the method of rates developed by Berardino et al. (2002). This method chooses a vector $\mathbf{m} = \mathbf{v}$ of rate parameters such that each element v_i represents the rate of change in displacement (i.e. velocity) between each pair of consecutive epochs (i.e. during the i^{th} interval of time). Given a set of n pairs and a vector \mathbf{t} of m epochs, we solve for a vector \mathbf{v} of $m - 1$ rate parameters using the Berardino design matrix $\mathbf{G}^{[B]}$ via the following procedure.

Step 1: Define an edge-vertex matrix Δ with $m - 1$ rows and m columns representing the edge-vertex incidence matrix corresponding to a path graph chronologically connecting all epochs in the data set. In our 2-component example, the path connects the two distinct components.

Step 2: Find the pair-rate matrix \mathbf{B} , where the i, j^{th} element $B_{i,j} = 1$ if the i^{th} pair corresponds to the j^{th} rate and $B_{i,j} = 0$ otherwise. This matrix can be calculated from the product of the incidence matrix \mathbf{Q} and the pseudoinverse Δ^\dagger of the edge-vertex matrix:

$$\mathbf{B} = \mathbf{Q}\Delta^\dagger \tag{3.9}$$

Here, we note that \mathbf{B} is itself an incidence matrix as it denotes the relationship between pairs and rates. We take the pseudoinverse of Δ because its rank deficient nature indicates it is not directly invertible.

Step 3: Define a diagonal $(m - 1)$ -by- $(m - 1)$ matrix \mathbf{T} with the time intervals between consecutive epochs as the diagonal elements and zeros as the off-diagonal elements:

$$T_{i,j} = \delta_{i,j}(t_{i+1} - t_i) \tag{3.10}$$

where $\delta_{i,j}$ is the Kronecker delta

$$\delta_{i,j} = \begin{cases} 0 & \text{if } i \neq j \\ 1 & \text{if } i = j \end{cases} \quad (3.11)$$

Step 4: Find the Berardino design matrix $\mathbf{G}_{n \times (m-1)}^{[B]}$ from the product of the pair-rate incidence matrix \mathbf{B} and the diagonal matrix of time intervals \mathbf{T} :

$$\mathbf{G}_{n \times (m-1)}^{[B]} = \mathbf{B}\mathbf{T} \quad (3.12)$$

Step 5: Estimate the vector of rate parameters \mathbf{v} by solving $\mathbf{G}^{[B]}\mathbf{v} = \mathbf{d}$ using singular value decomposition (SVD).

We note that this method fails when the data set includes more than one distinct tree because the system of equations is rank deficient. Thus, the minimum-norm solution given by the pseudoinverse in singular value decomposition will tend to oscillate. For example, we consider again the case graphed in Figure 1.1 (g) with $n = 3$ distinct pairs of displacements $\mathbf{d} = \{d_{1,2}, d_{3,4}, d_{4,5}\}$. We represent the epochs in chronological order as a vector $\mathbf{t} = \{t_1, t_2, t_3, t_4, t_5\}$. The data provide no information regarding the velocity $v_{2,3}$ during the interval between t_2 and t_3 . We begin by defining the edge-vertex matrix Δ for the path connecting all epochs:

$$\Delta = \begin{bmatrix} -1 & 1 & 0 & 0 & 0 \\ 0 & -1 & 1 & 0 & 0 \\ 0 & 0 & -1 & 1 & 0 \\ 0 & 0 & 0 & -1 & 1 \end{bmatrix} \quad (3.13)$$

We next solve for the pair-rate incidence matrix \mathbf{B} by equation (3.9) using the pseu-

inverse Δ^\dagger and the incidence matrix \mathbf{Q} from equation (3.1)

$$\mathbf{B} = \begin{bmatrix} -1 & 1 & 0 & 0 & 0 \\ 0 & 0 & -1 & 1 & 0 \\ 0 & 0 & 0 & -1 & 1 \end{bmatrix} \begin{bmatrix} \frac{-4}{5} & \frac{-3}{5} & \frac{-2}{5} & \frac{-1}{5} \\ \frac{1}{5} & \frac{-3}{5} & \frac{-2}{5} & \frac{-1}{5} \\ \frac{1}{5} & \frac{2}{5} & \frac{-2}{5} & \frac{-1}{5} \\ \frac{1}{5} & \frac{2}{5} & \frac{3}{5} & \frac{-1}{5} \\ \frac{1}{5} & \frac{2}{5} & \frac{3}{5} & \frac{4}{5} \end{bmatrix} \quad (3.14)$$

$$= \begin{bmatrix} 1 & 0 & 0 & 0 \\ 0 & 0 & 1 & 0 \\ 0 & 0 & 0 & 1 \end{bmatrix}$$

We write the diagonal time-interval matrix \mathbf{T} according to equation (3.10) as

$$\mathbf{T} = \begin{bmatrix} (t_2 - t_1) & 0 & 0 & 0 \\ 0 & (t_3 - t_2) & 0 & 0 \\ 0 & 0 & (t_4 - t_3) & 0 \\ 0 & 0 & 0 & (t_5 - t_4) \end{bmatrix} \quad (3.15)$$

Finally, we solve for $\mathbf{G}^{[B]}$ using equation (3.12):

$$\mathbf{G}^{[B]} = \mathbf{B}\mathbf{T}$$

$$= \begin{bmatrix} (t_2 - t_1) & 0 & 0 & 0 \\ 0 & 0 & (t_4 - t_3) & 0 \\ 0 & 0 & 0 & (t_5 - t_4) \end{bmatrix} \quad (3.16)$$

The system of equations now takes the form $\mathbf{G}^{[B]}\mathbf{v} = \mathbf{d}_{obs}$.

$$\begin{bmatrix} (t_2 - t_1) & 0 & 0 & 0 \\ 0 & 0 & (t_4 - t_3) & 0 \\ 0 & 0 & 0 & (t_5 - t_4) \end{bmatrix} \begin{bmatrix} v_{1,2} \\ v_{2,3} \\ v_{3,4} \\ v_{4,5} \end{bmatrix} = \begin{bmatrix} d_{1,2} \\ d_{3,4} \\ d_{4,5} \end{bmatrix} \quad (3.17)$$

where \mathbf{v} is the parameter vector of velocities and \mathbf{d}_{obs} is the vector of observed pairwise, relative displacements. The design matrix $\mathbf{G}^{[B]}$ has a rank deficiency of 1. Its null column indicates a lack of information during the time interval between epochs t_2 and t_3 . Consequently, the relative velocity $v_{2,3}$ between the two distinct trees (disconnected components) of the incidence graph (Figure 3.1 (c)) is unconstrained. In other words, the path graph described by Δ includes an edge $e_{2,3}$ that is not in the 2-component graph described by \mathbf{Q} .

Singular value decomposition gives a minimum-norm solution, assuming no movement where there is a lack of information. In general, the minimum-norm solution by SVD becomes more prone to local oscillations as the number of unconstrained parameters increases (Aster et al., 2013, pp. 75, 93). To alleviate the locally oscillatory nature of the minimum-length solution found through SVD of Berardino et al. (2002)'s method, we consider other regularizations. We recognize that the minimum-length least-squares solution of this method found from SVD is equivalent to the zeroth-order Tikhonov solution of Berardino et al. (2002) in the limit as the regularization parameter approaches zero.

Instead, we choose to impose first-order Tikhonov regularization using an $(m - 1)$ -by- m matrix \mathbf{W} that quantifies the flatness of the solution and a regularization parameter β (e.g., Aster et al., 2013). The purpose of the first-order roughening matrix \mathbf{W} is to favor constant-rate solutions. The regularization parameter β allows us to choose how

much we favor the minimum misfit over our desire for a constant-rate solution (and vice versa). To resolve this trade-off, we use an L-curve to compare the L2 norms of the model vectors with those of the residual vectors. Figure 3.1 (d) shows an application of first-order Tikhonov regularization to the Berardino et al. (2002) parameterization of our example case with the regularization parameter set to $\beta = 0.0090$. The regularized solution tends towards constant rates. We describe a practical example in Section 5.6 below.

3.3 Design Matrix \mathbf{G} for Other Functions of Time

Hetland et al. (2012) develop a “library” of functions to describe the time dependence of InSAR data. Following their approach, we formulate the design matrix \mathbf{G} to represent temporal functions that are more complicated than the piecewise-linear polynomials just presented. In these cases, we formulate our system of equations to represent the product of a vector of model parameters \mathbf{m} and a temporal function $f(t)$. This parameterization assumes that the time-dependent and spatial-dependent functions are separable. Thus, we consider only the time-dependent function in our analysis. We write an element of the design matrix \mathbf{G} corresponding to the j^{th} element of the model parameter m_j

$$G_{i,j} = f_j(t_{2,i}) - f_j(t_{1,i}) \quad (3.18)$$

where t_1 and t_2 refer to the first and second epochs of the i^{th} pair, respectively. Now we have a system of equations $\mathbf{G}\mathbf{m} = \mathbf{d}$ where \mathbf{m} is the vector of unknown parameters and \mathbf{d} is the vector of pair-wise data. If we choose the temporal function $f(t)$ wisely to reduce the number of parameters such that \mathbf{G} has full column rank, then constraints are not necessary to solve the least-squares problem. The parameter vector \mathbf{m} contains m elements indexed m_i . For example, we use a temporal function with a single parameter

m_1

$$mf_{\text{exp}}(t_i) = m_1 \left(1 - \exp \left[-\frac{t_i - t_q}{\tau_m} \right] \right) \quad (3.19)$$

to model our data set, where t_i is the j^{th} epoch, t_q is a predefined reference epoch and τ_m is a predefined characteristic time constant. The corresponding matrix equation $\mathbf{G}\mathbf{m} = \mathbf{d}$ becomes

$$\begin{bmatrix} \left(1 - \exp \left[-\frac{t_2 - t_q}{\tau_m} \right] \right) - \left(1 - \exp \left[-\frac{t_1 - t_q}{\tau_m} \right] \right) \\ \left(1 - \exp \left[-\frac{t_4 - t_q}{\tau_m} \right] \right) - \left(1 - \exp \left[-\frac{t_3 - t_q}{\tau_m} \right] \right) \\ \left(1 - \exp \left[-\frac{t_5 - t_q}{\tau_m} \right] \right) - \left(1 - \exp \left[-\frac{t_4 - t_q}{\tau_m} \right] \right) \end{bmatrix} \begin{bmatrix} m_1 \end{bmatrix} = \begin{bmatrix} d_{1,2} \\ d_{3,4} \\ d_{4,5} \end{bmatrix} \quad (3.20)$$

In practice, the values of parameters such as t_q and τ_m may not be known. In this case, we use nonlinear optimization in conjunction with the linear inversion problem to choose the best-fitting values of the parameters based on the residual misfit to the data, as described below in Section 5.7.

3.4 Defining the Data Covariance Matrix

To account for the measurement uncertainty in the temporal dimension of the observed data \mathbf{d} , we construct the data covariance matrix Σ_d . In the case of pair-wise InSAR data (unwrapped interferograms), the observed values of range change are given for the edges. We can employ what Merris (1994) calls the n -by- n edge-version of the Laplacian matrix

$$\mathbf{K} = \mathbf{Q}\mathbf{Q}^\top \quad (3.21)$$

where \mathbf{Q} again represents our edge-vertex incidence matrix.

Spielman (2010) defines the normalized edge Laplacian as

$$\mathbf{L} = \mathbf{D}^{-1/2} \mathbf{K} \mathbf{D}^{-1/2} \quad (3.22)$$

where the edge-degree matrix \mathbf{D} is an n -by- n square matrix with the degrees of the edges on the diagonal and zeros elsewhere (Harris et al., 2008). (Note that our \mathbf{D} is not the same as the incidence matrix denoted by the same symbol in Feigl and Thurber (2009).)

Each of the diagonal elements in the normalized edge Laplacian \mathbf{L} is unity. The off-diagonal elements are $\pm\frac{1}{2}$ for pairs sharing a common epoch and zero elsewhere. Thus, the matrix \mathbf{L} is the data correlation matrix (Merris, 1994). It is similar to the correlation matrix for a triangulation network composed of angles (differences of directions) measured by theodolite (e.g., Prescott, 1976). The off-diagonal elements of this data correlation matrix account for the temporal correlation between interferometric pairs sharing a common epoch. Two pairs of data have a correlation coefficient of $+\frac{1}{2}$ if they share a common first or second epoch, $-\frac{1}{2}$ if they share a common epoch but the epoch is first in one pair and second in the other, and zero otherwise. The correlation matrix \mathbf{L} leads to the corresponding n -by- n covariance matrix for pair-wise data:

$$\Sigma_d = \mathbf{SLS} \tag{3.23}$$

where \mathbf{S} is a diagonal matrix containing the standard deviation s of each measured pair.

This result derived from graph theory validates formulae presented by Hanssen (2001) in his equation (3.1.4). It also reformulates the results derived by Emardson et al. (2003) in their equation (31), Biggs et al. (2007) in their equation (5), and Agram and Simons (2015) in their equation (10). This graphical formulation of the data covariance matrix is necessary to derive the covariance matrix of relative epoch-wise errors, which is new to InSAR and described in further detail in Section 3.6.

3.5 Example Case: Data Covariance Matrix

Let us resume the example depicted in Figure 1.1 (g), containing five epochs $\{t_1, t_2, t_3, t_4, t_5\}$ corresponding to five vertices and $n = 3$ pairs $\{e_{1,2}, e_{3,4}, e_{4,5}\}$ in $k = 2$ distinct trees. Given the incidence matrix \mathbf{Q} (in equation (3.1)), we first calculate the 3-by-3 edge Laplacian using equation (3.21).

$$\begin{aligned}
 \mathbf{K} &= \mathbf{Q}\mathbf{Q}^\top \\
 &= \begin{bmatrix} -1 & 1 & 0 & 0 & 0 \\ 0 & 0 & -1 & 1 & 0 \\ 0 & 0 & 0 & -1 & 1 \end{bmatrix} \begin{bmatrix} -1 & 0 & 0 \\ 1 & 0 & 0 \\ 0 & -1 & 0 \\ 0 & 1 & -1 \\ 0 & 0 & 1 \end{bmatrix} \\
 &= \begin{bmatrix} 2 & 0 & 0 \\ 0 & 2 & -1 \\ 0 & -1 & 2 \end{bmatrix}
 \end{aligned} \tag{3.24}$$

To write the normalized edge Laplacian \mathbf{L} , we also need the edge-degree matrix \mathbf{D} . We sum the absolute values of the elements in each row of the edge-vertex incidence matrix \mathbf{Q} and diagonalize the result into a 3-by-3 matrix:

$$\mathbf{D} = \begin{bmatrix} 2 & 0 & 0 \\ 0 & 2 & 0 \\ 0 & 0 & 2 \end{bmatrix} \tag{3.25}$$

From equation (3.22), the correlation matrix is:

$$\begin{aligned}
\mathbf{L} &= \mathbf{D}^{-\frac{1}{2}} \mathbf{K} \mathbf{D}^{-\frac{1}{2}} \\
&= \begin{bmatrix} \frac{1}{\sqrt{2}} & 0 & 0 \\ 0 & \frac{1}{\sqrt{2}} & 0 \\ 0 & 0 & \frac{1}{\sqrt{2}} \end{bmatrix} \begin{bmatrix} 2 & 0 & 0 \\ 0 & 2 & -1 \\ 0 & -1 & 2 \end{bmatrix} \begin{bmatrix} \frac{1}{\sqrt{2}} & 0 & 0 \\ 0 & \frac{1}{\sqrt{2}} & 0 \\ 0 & 0 & \frac{1}{\sqrt{2}} \end{bmatrix} \\
&= \begin{bmatrix} 1 & 0 & 0 \\ 0 & 1 & -\frac{1}{2} \\ 0 & -\frac{1}{2} & 1 \end{bmatrix}
\end{aligned} \tag{3.26}$$

Finally, we use equation (3.23) to find the data covariance matrix Σ_d . Writing the pair-wise measurement errors as a diagonal matrix $\mathbf{S} = \text{diag}(s_{1,2}, s_{3,4}, s_{4,5})$, we find the covariance of the pair-wise data

$$\begin{aligned}
\Sigma_d &= \begin{bmatrix} s_{1,2} & 0 & 0 \\ 0 & s_{3,4} & 0 \\ 0 & 0 & s_{4,5} \end{bmatrix} \begin{bmatrix} 1 & 0 & 0 \\ 0 & 1 & -\frac{1}{2} \\ 0 & -\frac{1}{2} & 1 \end{bmatrix} \begin{bmatrix} s_{1,2} & 0 & 0 \\ 0 & s_{3,4} & 0 \\ 0 & 0 & s_{4,5} \end{bmatrix} \\
&= \begin{bmatrix} s_{1,2}^2 & 0 & 0 \\ 0 & s_{3,4}^2 & -\frac{s_{3,4}s_{4,5}}{2} \\ 0 & -\frac{s_{3,4}s_{4,5}}{2} & s_{4,5}^2 \end{bmatrix}
\end{aligned} \tag{3.27}$$

The data covariance matrix Σ_d can be inverted because a Laplacian matrix is necessarily positive semi-definite (Merris, 1994).

3.6 Epoch-wise Covariance

In the previous section, we introduced a formulation for the covariance matrix of (pair-wise) data. Now we use that formulation to estimate the relative covariance matrix

for epoch-wise measurements. Given the edge-vertex incidence matrix \mathbf{Q} and assuming a covariance matrix Σ_ρ for the epoch-wise measurements, we can use the principle of covariance propagation (e.g., equation (2.22) of Aster et al., 2013) to write the covariance matrix Σ_d of the pair-wise data:

$$\Sigma_d = \mathbf{Q}\Sigma_\rho\mathbf{Q}^\top \quad (3.28)$$

Setting the two expressions (3.23) and (3.28) for the pairwise covariance Σ_d equal to each other, we find

$$\mathbf{Q}\Sigma_\rho\mathbf{Q}^\top = \mathbf{S}\mathbf{L}\mathbf{S} \quad (3.29)$$

Since neither \mathbf{Q} nor \mathbf{Q}^\top is a square matrix, we cannot invert them. However, we can manipulate these matrices using \mathbf{Q}^\top and \mathbf{Q} , respectively, to rewrite equation (3.29) in terms of square matrices:

$$\mathbf{Q}^\top\mathbf{Q}\Sigma_\rho\mathbf{Q}^\top\mathbf{Q} = \mathbf{Q}^\top\mathbf{S}\mathbf{L}\mathbf{S}\mathbf{Q} \quad (3.30)$$

We can now multiply by the inverse of $(\mathbf{Q}^\top\mathbf{Q})$

$$\begin{aligned} (\mathbf{Q}^\top\mathbf{Q})^{-1}(\mathbf{Q}^\top\mathbf{Q})\Sigma_\rho(\mathbf{Q}^\top\mathbf{Q})(\mathbf{Q}^\top\mathbf{Q})^{-1} = \\ (\mathbf{Q}^\top\mathbf{Q})^{-1}\mathbf{Q}^\top\mathbf{S}\mathbf{L}\mathbf{S}\mathbf{Q}(\mathbf{Q}^\top\mathbf{Q})^{-1} \end{aligned} \quad (3.31)$$

to arrive at an equation representing the covariance of the epoch-wise measurements

$$\Sigma_\rho = (\mathbf{Q}^\top\mathbf{Q})^{-1}\mathbf{Q}^\top\mathbf{S}\mathbf{L}\mathbf{S}\mathbf{Q}(\mathbf{Q}^\top\mathbf{Q})^{-1} \quad (3.32)$$

Equation (3.32) is equivalent to the general covariance matrix of model parameters for a least-squares solution (e.g., Aster et al., 2013, p. 31). However, for the n -by- m edge-vertex incidence matrix \mathbf{Q} , its inverse $(\mathbf{Q}^\top\mathbf{Q})^{-1}$ strictly does not exist. If we regularize the incidence matrix by adding a constraint of zero mean for each component, then we

can examine the relative uncertainty of the epoch-wise measurements. This is equivalent to setting the epoch-wise errors in each component to have a mean of zero. To do so, we include k more equations to the system of equations corresponding to the k components of the data set. The modified system of equations is

$$\mathbf{Q}'\mathbf{m} = \begin{bmatrix} \mathbf{Q} \\ \mathbf{C} \end{bmatrix} \mathbf{m} = \begin{bmatrix} \mathbf{d} \\ 0 \end{bmatrix} = \mathbf{d}' \quad (3.33)$$

Here, we have appended k zeros to the data vector \mathbf{d} and a k -by- m constraint matrix \mathbf{C} to the edge-vertex incidence matrix \mathbf{Q} . The constraint matrix \mathbf{C} consists of non-zero elements $C_{i,j} = 1/\eta_i$ when j is the index of an epoch belonging to the i^{th} component. The integer η_i is the number of epochs in the i^{th} component. Similarly, we append k elements having a weight of unity to the vector of uncertainties \mathbf{s} of the pair-wise measurements to arrive at a new vector \mathbf{s}' . Here we arbitrarily choose a weight of unity, although we could also represent equation (3.33) in a Tikhonov framework and solve for the weight according to trade-off between the norm of the residual and the norm of the model. We employ these appended matrices using the methods outlined in section 3.4 to arrive at a new $(n+k)$ -by- $(n+k)$ covariance matrix for the pair-wise data

$$\Sigma'_d = \mathbf{Q}'\Sigma'_\rho\mathbf{Q}'^\top \quad (3.34)$$

Next, we solve for the covariance matrix containing the relative uncertainties of the epoch-wise measurements by substituting \mathbf{Q}' and Σ'_d for \mathbf{Q} and Σ_d , respectively, in equation (3.32):

$$\Sigma'_\rho = (\mathbf{Q}'^\top\mathbf{Q}')^{-1}\mathbf{Q}'^\top\Sigma'_d\mathbf{Q}'(\mathbf{Q}'^\top\mathbf{Q}')^{-1} \quad (3.35)$$

The diagonal elements of this matrix lead to a vector of relative uncertainties of the

epoch-wise measurements

$$\boldsymbol{\sigma}_\rho = \text{diag}(\boldsymbol{\Sigma}'_\rho)^{1/2} \quad (3.36)$$

We can also represent the corresponding correlation matrix of the epoch-wise measurements as

$$\mathbf{L}_\rho = \mathbf{D}_\rho^{-1/2} \boldsymbol{\Sigma}'_\rho \mathbf{D}_\rho^{-1/2} \quad (3.37)$$

where \mathbf{D}_ρ is the $(n+k)$ -by- $(n+k)$ vertex-degree matrix defined similarly to its counterpart, the edge-degree matrix \mathbf{D} , as discussed in Section 3.4.

We continue with our simple example case of five epochs $\{t_1, t_2, t_3, t_4, t_5\}$ and $n = 3$ pairs $\{e_{1,2}, e_{3,4}, e_{4,5}\}$ in $k = 2$ distinct components, such that epochs t_1 and t_2 are vertices in the first component and epochs t_3, t_4 , and t_5 are vertices in the second component (see Figure 1.1 (g)). We start by defining our constraint matrix \mathbf{C} from equation (3.33):

$$\mathbf{C} = \begin{bmatrix} \frac{1}{2} & \frac{1}{2} & 0 & 0 & 0 \\ 0 & 0 & \frac{1}{3} & \frac{1}{3} & \frac{1}{3} \end{bmatrix} \quad (3.38)$$

where \mathbf{C} has 2 rows corresponding to the number of trees and the denominators of the fractional elements correspond to the number of epochs in each component, such that $\eta_1 = 2$ and $\eta_2 = 3$. We now can write the new system of equations $\mathbf{Q}'\mathbf{m} = \mathbf{d}'$ as

$$\begin{bmatrix} -1 & 1 & 0 & 0 & 0 \\ 0 & 0 & -1 & 1 & 0 \\ 0 & 0 & 0 & -1 & 1 \\ \frac{1}{2} & \frac{1}{2} & 0 & 0 & 0 \\ 0 & 0 & \frac{1}{3} & \frac{1}{3} & \frac{1}{3} \end{bmatrix} \begin{bmatrix} m_1 \\ m_2 \\ m_3 \\ m_4 \\ m_5 \end{bmatrix} = \begin{bmatrix} d_{1,2} \\ d_{3,4} \\ d_{4,5} \\ 0 \\ 0 \end{bmatrix} \quad (3.39)$$

We also define a matrix \mathbf{S}' to include the uncertainty of the pair-wise data and the

constraints:

$$\mathbf{S}' = \begin{bmatrix} s_{1,2} & 0 & 0 & 0 & 0 \\ 0 & s_{3,4} & 0 & 0 & 0 \\ 0 & 0 & s_{4,5} & 0 & 0 \\ 0 & 0 & 0 & 1 & 0 \\ 0 & 0 & 0 & 0 & 1 \end{bmatrix} \quad (3.40)$$

Using equation (3.23), we modify the covariance matrix of pair-wise data Σ'_d :

$$\Sigma'_d = \begin{bmatrix} s_{1,2}^2 & 0 & 0 & 0 & 0 \\ 0 & s_{3,4}^2 & -\frac{s_{3,4}s_{4,5}}{2} & 0 & 0 \\ 0 & -\frac{s_{3,4}s_{4,5}}{2} & s_{4,5}^2 & 0 & 0 \\ 0 & 0 & 0 & \frac{1}{2} & 0 \\ 0 & 0 & 0 & 0 & \frac{1}{3} \end{bmatrix} \quad (3.41)$$

Defining an example set of pair-wise measurement uncertainties such that $s_{1,2} = s_{3,4} = s_{4,5} = 1$ (mm), we can use equation (3.32) along with the substitutions in equations (3.33) and (3.34) to arrive at the covariance matrix of relative epoch-wise measurements:

$$\Sigma_\rho = \begin{bmatrix} \frac{3}{4} & \frac{1}{4} & 0 & 0 & 0 \\ \frac{1}{4} & \frac{3}{4} & 0 & 0 & 0 \\ 0 & 0 & \frac{2}{3} & \frac{1}{6} & \frac{1}{6} \\ 0 & 0 & \frac{1}{6} & \frac{2}{3} & \frac{1}{6} \\ 0 & 0 & \frac{1}{6} & \frac{1}{6} & \frac{2}{3} \end{bmatrix} \text{ (mm)} \quad (3.42)$$

3.7 Least-Squares Solution Using the Pseudoinverse and Normal Equations

Having defined the data covariance matrix, the design matrix, and the model parameters, we can represent the weighted least-squares problem as minimizing the objective function

$$f_{obj}(\mathbf{d}; \mathbf{m}) = (\mathbf{G}\mathbf{m} - \mathbf{d})\boldsymbol{\Sigma}_d^{-1}(\mathbf{G}\mathbf{m} - \mathbf{d}) \quad (3.43)$$

To solve the weighted least-squares problem, we use the pseudoinverse:

$$\tilde{\mathbf{m}} = (\mathbf{G}^\top \boldsymbol{\Sigma}_d^\dagger \mathbf{G})^\dagger \mathbf{G}^\top \boldsymbol{\Sigma}_d^\dagger \mathbf{d} \quad (3.44)$$

Since the two pseudoinverses always exist, the solution expressed in equation (3.44) determines a unique set of estimates for the model parameters.

To quantify the misfit, we calculate the mean squared error (MSE) of the fit, or variance of unit weight, from the scatter of the weighted residuals as (Strang and Borre, 1997):

$$\sigma_0^2 = \frac{\mathbf{r}^\top \boldsymbol{\Sigma}_d^\dagger \mathbf{r}}{n_G - m_G} \quad (3.45)$$

where the vector $\mathbf{r} = \mathbf{d} - \mathbf{G}\tilde{\mathbf{m}}$ refers to the residuals, and n_G and m_G refer to the number of rows and columns of \mathbf{G} , respectively, and $\nu = n_G - m_G$ refers to the degrees of freedom of the system.

The MSE is also called the reduced chi-squared statistic χ^2 (e.g., Aster et al., 2013). The scaled variance of the model parameters is

$$\boldsymbol{\Sigma}_m = \sigma_0^2 (\mathbf{G}^\top \boldsymbol{\Sigma}_d^\dagger \mathbf{G})^\dagger \quad (3.46)$$

The estimated standard deviations of the model parameters are thus

$$\boldsymbol{\sigma}_m = \sqrt{\text{diag}(\boldsymbol{\Sigma}_m)} \quad (3.47)$$

3.8 Applying the Forward Model

After calculating the solution to the temporal adjustment inverse problem, we apply the corresponding forward model to calculate the modeled values of displacement \mathbf{d}_{mod} . We then integrate the corresponding temporal function $f(t)$ over time to calculate the accumulated modeled displacement at each epoch in each tree. These values can then be plotted as a function of time. The constant of integration is arbitrarily assumed to be zero, thus setting $f(t_1) = 0$.

4 Implementation

We have implemented the method described in Section 3 using MATLAB (2014). Our source code is available free of charge and can be found on GitHub under the General Inversion of Phase Technique (GIPhT) suite (<https://github.com/feigl/gipht>). It is licensed under the GNU Lesser General Public License. The accompanying documentation includes figures showing all of the solutions discussed here

(<https://uwmadison.app.box.com/files/0/f/4061526069/GIPhTBox>).

4.1 Description of Functions

incidence_to_cov.m Given the edge Laplacian matrix \mathbf{L} of the data, the function *incidence_to_cov.m* calculates the data covariance matrix according to equations (22) through (24) of Section 3.4.

pinveb.m The function *pinveb.m* computes the pseudoinverse of a matrix using singular value decomposition and returns its condition number. An input argument specifies a threshold for truncating the singular values; otherwise a default tolerance is used. Alternatively, one can specify the number of singular values to include in the solution. This function also plots the spectrum of singular values.

ls_with_cov.m The function *ls_with_cov.m* computes the solution to the weighted least-squares problem using the pseudoinverse via equations (44) through (47) in Section 3.7.

findtrees.m The function *findtrees.m* finds and counts the distinct trees of a data set using the rank deficiency μ of the system and the rational basis of the null space of \mathbf{Q} found from the reduced row echelon form.

plottrees.m The function *plottrees.m* plots the graph of the data set as distinct trees (e.g., Figure 5.6).

5 Application to Okmok Volcano

Temporal adjustment also applies to parameters in a geophysical model, such as the increase in volume of a magma chamber beneath a volcano (e.g., Lu and Dzurisin, 2014; Feigl et al., 2014; Le Mével et al., 2015a). As a practical example, we apply our method of temporal adjustment to InSAR data collected from Okmok volcano in Alaska.

5.1 Background of Okmok Volcano

Here we quote Ohlendorf (2015) for a summary of geodetic studies at Okmok Volcano.

A number of geodetic studies have attempted to characterize the Okmok magma chamber, and these have revealed several problems regarding the consistency and plausibility of the estimates of its properties. Discrepancies in the chamber depth exist between different types of studies in the fields of seismology, geodesy, and petrology, as summarized by Masterlark et al. (2010) and Ohlendorf et al. (2014)...

Work done over the past ten years, using different combinations of campaign GPS, continuous GPS, and InSAR data and covering various time periods, has typically found inflation/deflation source depths of 2-4 km below sea level. These deformation centers are assumed to correspond with magma storage zones, which inflate with magma influx and deflate when magma erupts or migrates to a different area. Freymueller and Kaufman (2010) also detected deflation of an additional pressure source at mid crustal depths after the 2008 eruption, concurrent with inflation of a shallow source at 2 km depth, presumably due to magma recharge from below. The simplest deformation model assumes a spherical source embedded in an elastic rheology with uniform material properties everywhere in a half space (Mogi, 1958; Segall, 2010). Several of the geodetic studies initially allowed the source to vary in location (e.g., Fournier et al., 2009) and/or varied the shape of the source from a sphere to a spheroid (e.g., Lu et al., 2010), but these additional degrees of freedom did not result in a significantly better fit to the data.... All of the favored models produced by the geodetic studies were derived by approximating the shallow pressure source as a spherical source (Mogi, 1958) in a homogeneous elastic half-space with uniform values of Poisson's ratio.... [T]he previous geodetic models, which assume a homogeneous elastic medium, derive much shallower depth estimates than that determined using a heterogeneous distribution of elastic material properties (Masterlark et al., 2010). Several of these studies also constructed time series showing the estimated source strength or pressure change of the magma source, often converted to source volume change through a series of assumptions about the source geometry and the compress-

ibility of the country rock. The time series shown in Fournier et al. (2009) and Lu et al. (2010) display fluctuations in [the] estimated magma influx rate over the 1997-2008 inter-eruptive period, including intervals of relatively rapid inflation from about 1997-2000 and 2002-2004, and a distinct flattening about 2004.

Figure 5.1 sketches a cross-section of Okmok Volcano. The model attributed to Mogi (1958) and described by Segall (2010) which formulates geodetic data in terms of a spherical source in a half-space with uniform values of the elastic properties is shown in Figure 5.2 (Figure 7.4 from Segall, 2010). Figure 5.3 is an example sketch from Fournier et al. (2009) (their Figure 12) comparing magma influx rate to cumulative volume change.

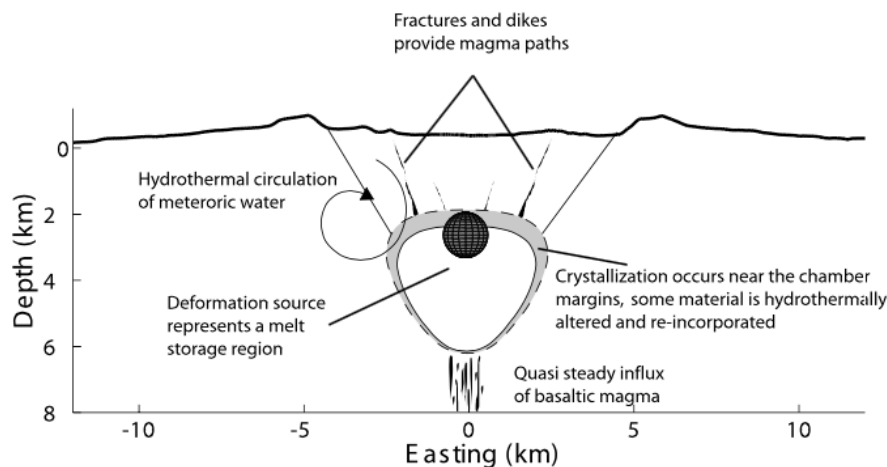


Figure 5.1: “Schematic cross section through Okmok that shows the deformation source located beneath the center of the caldera. The spherical source is drawn with a radius of ~ 500 m and is only meant to indicate the location and finite region that the true source occupies. The true size and dimensions of the magma chamber are unknown. Conical fractures emanating from the magma storage region provide pathways to the cones in the caldera. Petrologic work by Finney et al. [2008] suggests that hydrothermal alteration occurs in crystals that accumulate near the chamber margins.” Figure and caption from Fournier et al. (2009, their Figure 13)

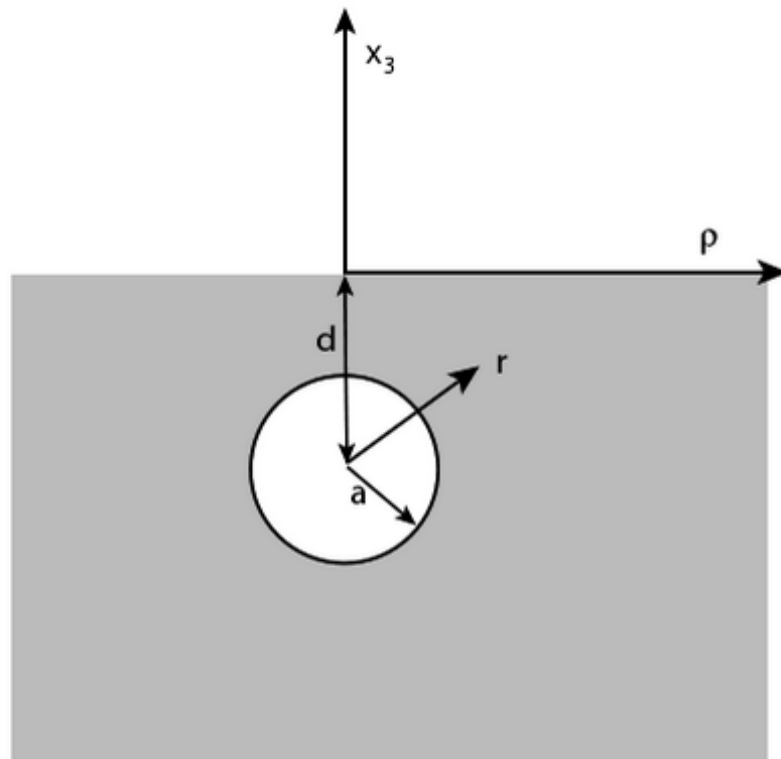


Figure 5.2: Sketch of “Mogi” model showing, in cross-section, “Geometry of a spherical magma chamber. The chamber has radius a , with center at depth d beneath the free surface, $x_3 = 0$. r denotes the radial distance from the center of the magma chamber, whereas ρ marks the distance from the center of symmetry along the free surface.” Figure and caption from Segall (2010, his Figure 7.4 on p. 203)

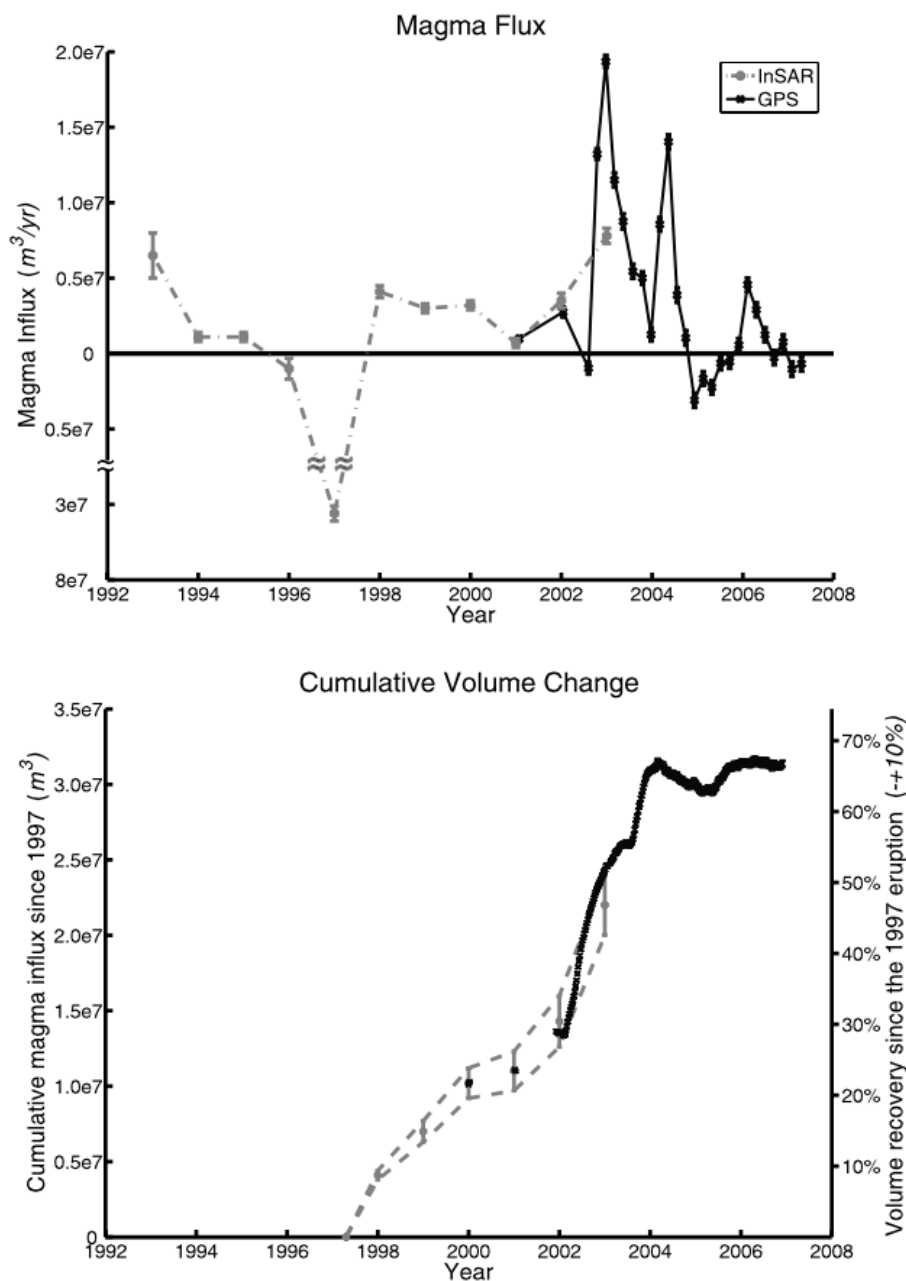


Figure 5.3: “Modified from Lu et al. (2005, Figure 9). (top) The rate of volume change from InSAR (gray) and GPS (black). There is good agreement in the rates for the years 2000 and 2001. The discrepancy in 2003 can be attributed to poor temporal sampling of InSAR which only shows the yearly averaged rate. The horizontal line distinguishes inflation (above) from deflation (below). (bottom) The total volume change estimated from InSAR (gray) since the 1997 eruption with the volume change estimates from GPS (black) overlying. The total volume recovered is $\sim 60\%$ – 80% of the volume lost during the 1997 eruption.” Figure and caption from Fournier et al. (2009, their Figure 12)

5.2 Setting up the Inverse Problem

The data set analyzed by Lu et al. (2005) includes SAR images acquired between July 1, 1997 and September 9, 2003 by four satellite missions: ERS-1, ERS-2, Radarsat-1, and JERS-1 (see Figure 5.4 for example interferograms from Lu et al. (2005, their Figure 3)). Although images acquired by ERS-1 form useful interferometric pairs with images

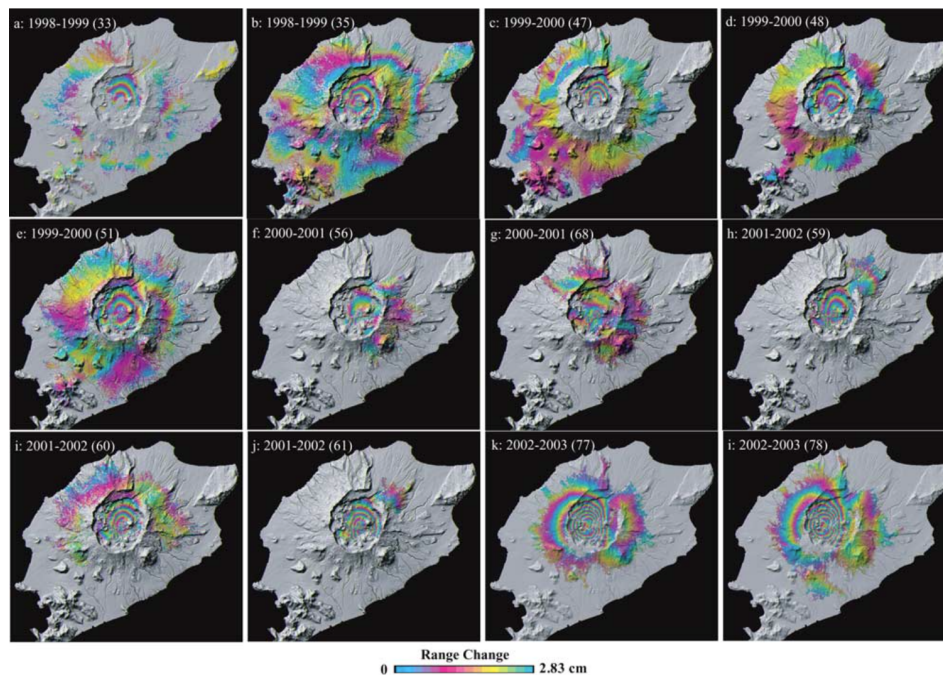


Figure 5.4: “Examples of interferograms showing progressive reinflation of Okmok volcano after its 1997 eruption. Each interferogram spans a time interval of about 1-year. Each fringe (full color cycle) represents 2.83 cm of range change between the ground and the satellite. Additional information on SAR images used to produce the interferograms is given in Table 1. Areas that lack interferometric coherence are uncolored.” Figure and caption from Lu et al. (2005, their Figure 3)

acquired by ERS-2, other heterogeneous combinations do not form useful pairs. The data set of 45 epochs yields 44 interferometric pairs (Appendix B). For each of them, Lu et al. (2005) estimate the parameters in the Mogi model. We use these estimates of the volumetric rate of change to form our data set for inversion (Figure 5.5). In other words, their output is our input. We convert their rates to differential volumes by multiplying

each rate by its corresponding interval of time. This approach assumes that the time-dependent and position-dependent parts of the displacement field are separable (e.g., Feigl and Thurber, 2009).

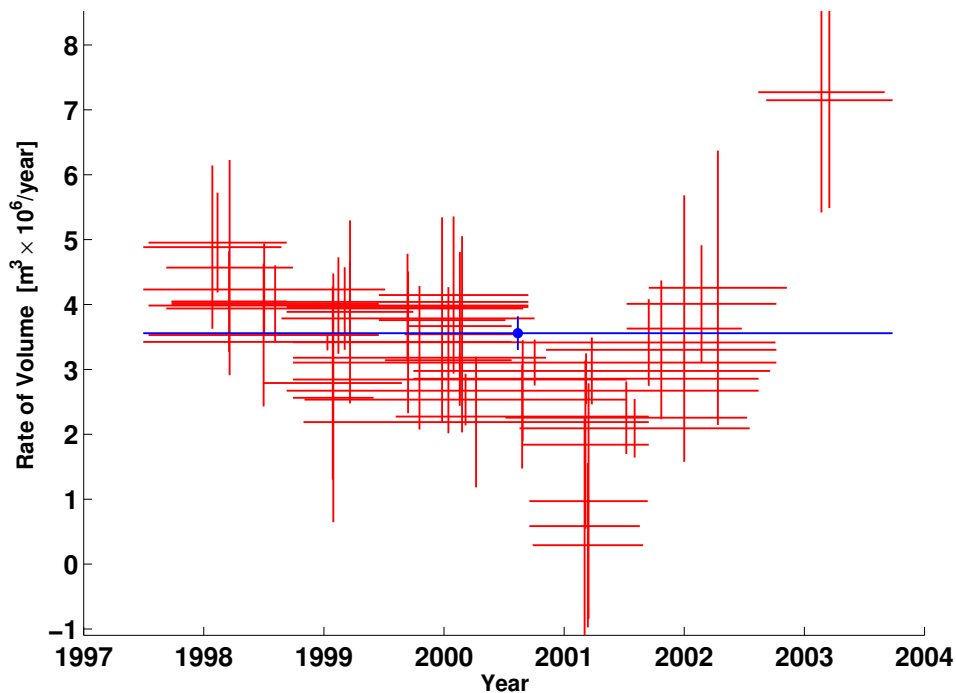


Figure 5.5: Rates of change in volume as a function of time for a modeled spherical magma chamber below Okmok volcano, as estimated from the 44 individual pairs of InSAR data (Red symbols) and their weighted mean (blue symbols). Horizontal segments indicate observed time intervals. Vertical bars indicate the (unscaled) interval of 68 percent confidence calculated from the RMSE values of the pair-wise solutions, as described in the text. Data from Table 1 of Lu et al. (2005) and reprinted with uncertainties in Appendix B.

Lu et al. (2005) do not give uncertainties for their estimates. To set the *a priori* standard deviation of each datum, we weight each estimate in a relative sense. For each pair, we normalize the root mean squared error (RMSE) of the residuals (as given by Lu et al. (2005)) by the mean of the RMSE values averaged over all 44 pairs and multiplied by an arbitrary, constant scale factor of $\sim 10^6$ m³/yr corresponding to the scale of the volumetric rates.

The graph of the data set includes $k = 10$ distinct components. Figure 5.6 shows the

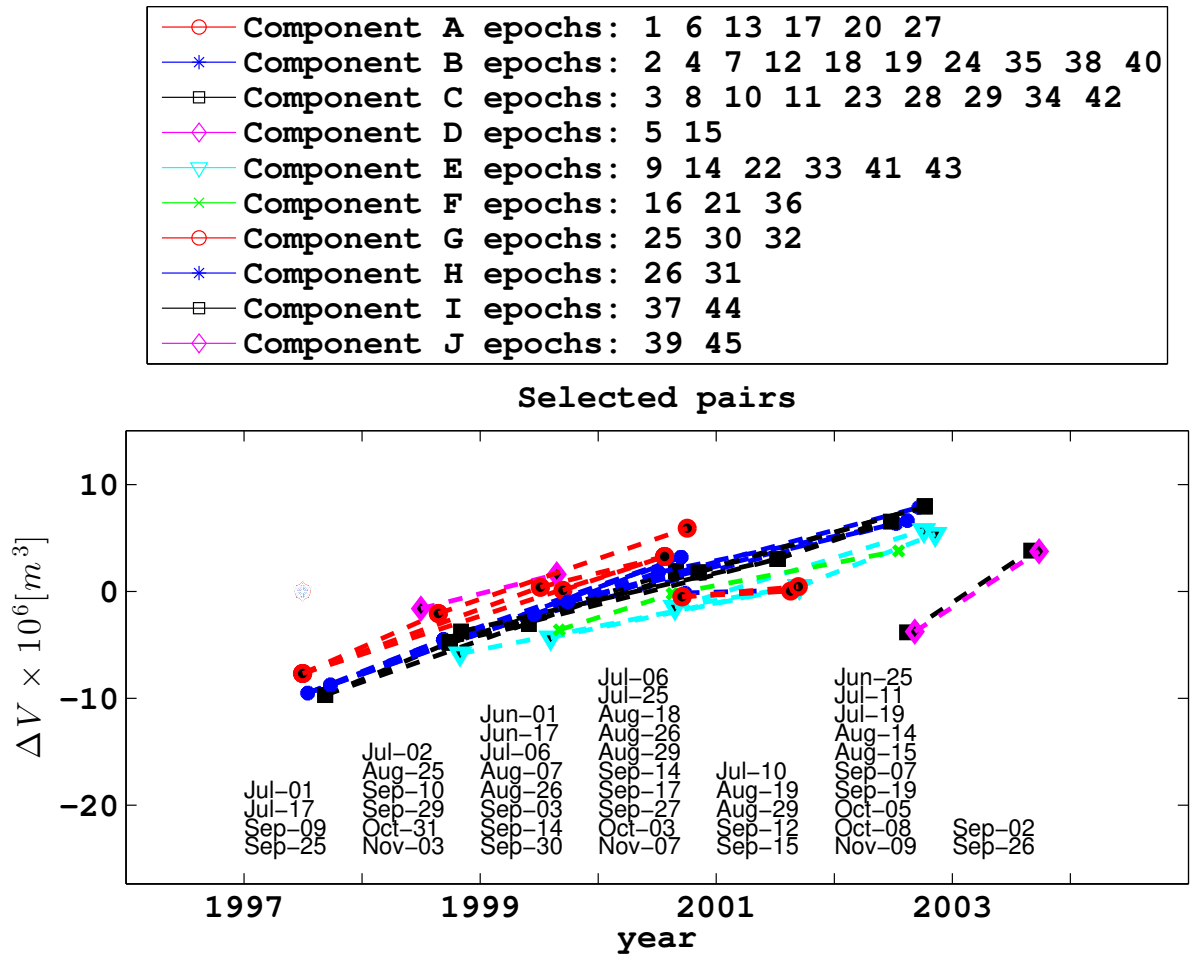


Figure 5.6: Plot of volume change for each pair as a function of time, showing epochs as dots and pairs as line segments connecting them. The calendar date for each epoch is listed in chronological order within each year.

volume change for each pair as a function of time, as calculated by `findtrees.m` and plotted by `plottrees.m`.

Graphing the data groups them naturally into subsets according to the sensors. For example, pairs of SAR images acquired by the ERS-2 satellite mission fall into components A through F, whereas images acquired by the RADARSAT-1 satellite fall into components G through J. Images are further separated into components by tracks. In estimating the model parameters, Lu et al. (2005) account for the different imaging configurations (e.g. incidence angle, radar wavelength) for each pair individually.

5.3 Estimation of Epoch-wise Variance

Using equation (3.35), we calculate the relative covariance matrix of the epoch-wise measurements. By taking the square root of the diagonal elements of this covariance matrix, we are able to determine the uncertainty of each of the individual, epoch-wise measurements. A plot of these values is shown in Figure 5.7. The largest relative uncertainties occur at epochs during the winter season, during which snow on the ground, precipitation, and/or moisture in the atmosphere are common in Alaska. These effects tend to degrade the quality of the interferogram, and thus the overall misfit of the modeled phase values to the observed values, found by Lu et al. (2005).

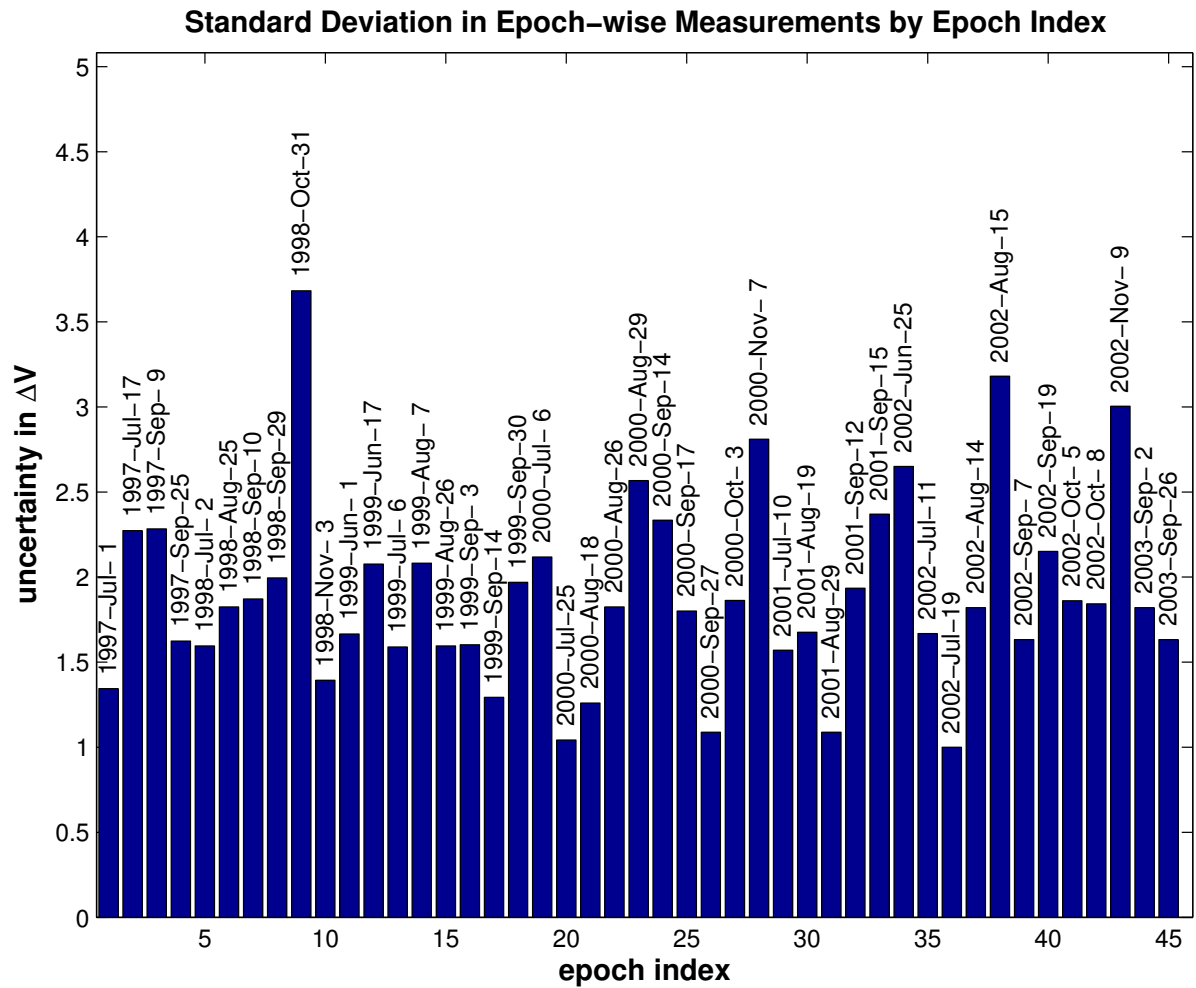


Figure 5.7: Bar graph of relative standard deviations in epoch-wise measurements as determined from the formulation in Section 3.6. The relative standard deviations are normalized by the smallest deviation. Each bar is labeled with the corresponding calendar date of the epoch.

5.4 Single-segment Secular Rate Parameterization

We consider six different parameterizations for the temporal adjustment. To save space, we show plots for only four of them in this paper. Plots for all the examples appear in the documentation for the GraphTreeTA software that is available at GitHub. The simplest parameterization is a constant-rate (secular) parameterization with a single-element parameter vector \mathbf{m} . Following the method outlined in Section 3.3, we construct the design matrix \mathbf{G} with a temporal function where t_0 is the initial epoch. Using the $n = 44$ pair-wise data, we find a good fit with misfit $\sigma_0 = 1.0226 \text{ m}^3$. The results are shown in Figure 5.8.

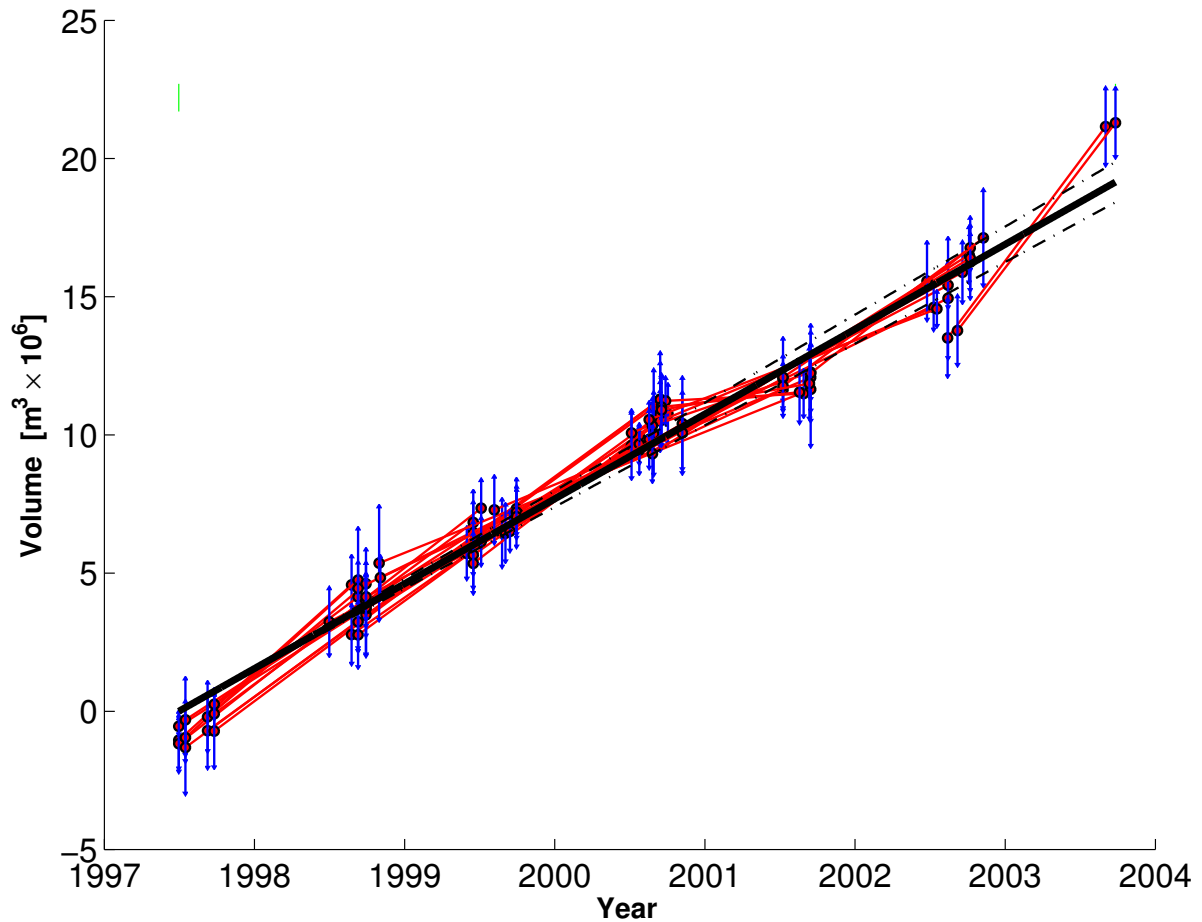


Figure 5.8: Volume increase as a function of time as estimated by temporal adjustment using a single-parameter model for a constant (secular) rate. Black lines show modeled value (solid line) with the envelope of 69 percent confidence, after scaling by σ_0 . The green tick represents the reference epoch. Red segments indicate the differential change in volume estimated from individual pairs. For each pair, the volume at the mid-point of the time interval is plotted to fall on the modeled curve. The estimated volume for each pair is plotted with its associated uncertainty (vertical blue bars). The length of each blue bar is set *a posteriori* to the 68-percent confidence interval for the pair after scaling by $\sigma_0/\sqrt{2}$, where $\sigma_0 = 1.0226 \text{ m}^3$.

5.5 Five-segment Piecewise-linear Parameterization

We expand the linear parameterization by adding 5 segments delimited by a 6-element vector of break points \mathbf{t}_b containing a break on January 1st of each year from 1999 to 2002, inclusive. The temporal function becomes piecewise-linear:

$$m_j f_{5seg}^{(j)}(t_i) = m_j \begin{cases} (t_i - t_{b_j}) & \text{if } t_{b_j} \leq t_i < t_{b_{j+1}} \\ (t_{b_{j+1}} - t_{b_j}) & \text{if } t_i \geq t_{b_{j+1}} \\ 0 & \text{otherwise} \end{cases} \quad (5.1)$$

This expression defines a 5-element parameter vector \mathbf{m} , where m_j describes the rate for the j^{th} interval, and a design matrix \mathbf{G} with 5 columns. The element $G_{i,j}$ stores the value of $f_{5seg}(t_i)$ evaluated for the i^{th} epoch and the j^{th} segment. This solution includes 5 rates and a misfit of $\sigma_0 = 0.4034 \text{ m}^3$, as seen in Figure 5.9. This figure essentially reproduces the result of Lu and Dzurisin (2014) (their Figure 6.98).

We find a better fit using 5 segments than using the constant (secular) rate parameterization. To decide if the additional complexity is justified, we perform an F test (e.g., Wackerly et al., 2007). The null hypothesis states that the two sets of weighted residuals (the observed minus calculated values of the differential volumes normalized by their corresponding measurement uncertainties) have equal variance. Comparing the secular rate and 5-segment models, we find $F = 36.07$. Since the critical value of the F statistic for a significance level of $\alpha = 0.05$ and degrees of freedom $\nu_1 = n - 1 = 43$ and $\nu_2 = n - 5 = 39$ (where n is the number of calculated residuals) is $F_{\alpha, \nu_1, \nu_2} = 1.69$, the null hypothesis is rejected with 95% confidence. We conclude that the 5-segment model provides an appropriate level of complexity.

In addition, we perform a two-tailed student t-test to decide whether or not the rates estimated during successive intervals of the 5-segment model show significant differences

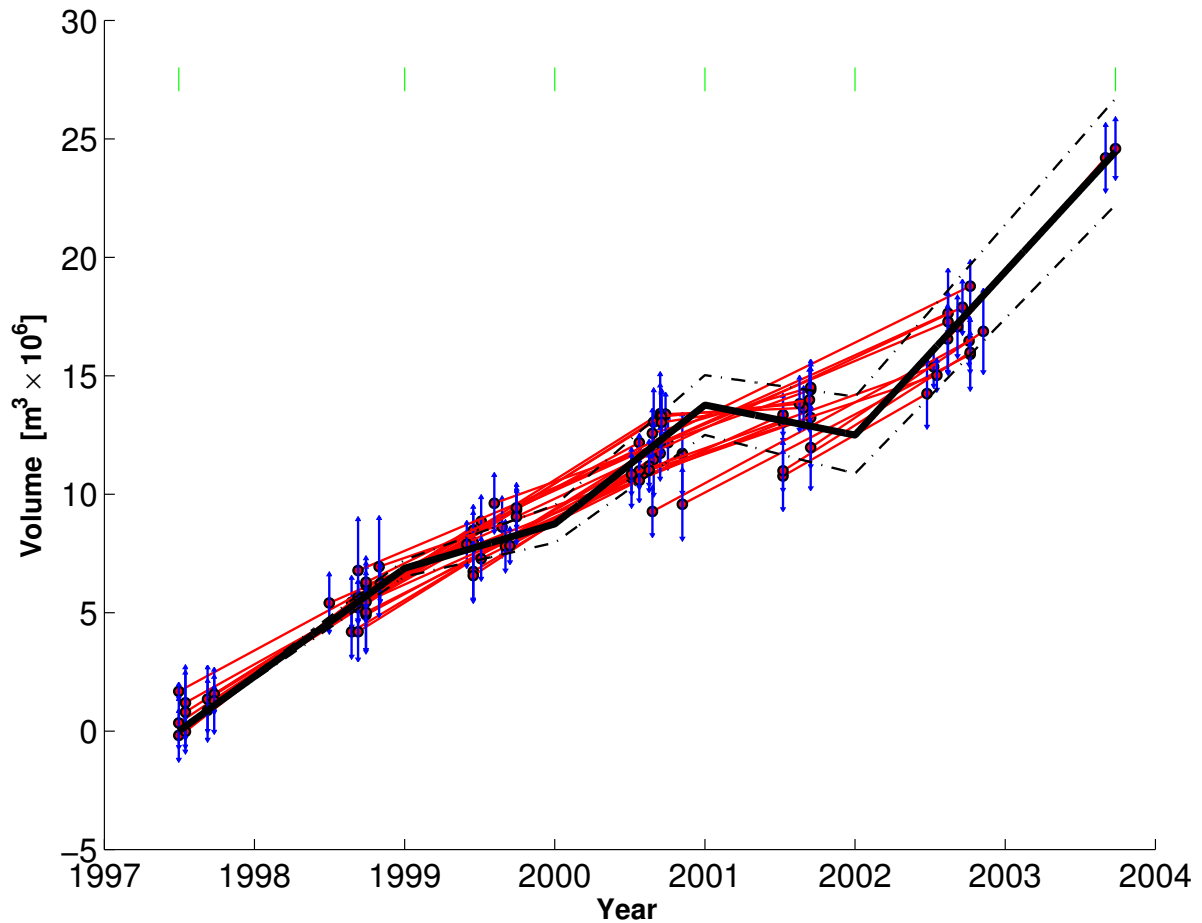


Figure 5.9: Volume increase as a function of time as estimated by temporal adjustment using the 5-segment piecewise-linear parametrization with yearly breaks from January 1, 1999 to January 1, 2002. The green ticks represent epochs separating time intervals. Misfit $\sigma_0 = 0.4034 \text{ m}^3$. This figure corresponds with Figure 6.98 of Lu and Dzurisin (2014). Plotting conventions as in previous figure.

(e.g., Wackerly et al., 2007). The null hypothesis states that the mean rates during the successive year-long intervals before and after January 1st of the tested year are equal. We set the significance level at $\alpha = 0.05$. We find that the value of the test statistic lies outside the acceptance interval $[-T_{\alpha/2}, +T_{\alpha/2}]$ formed by the corresponding values of $\pm T_{\alpha/2}$ for each year. Thus, the five estimated rates are distinguishable.

5.6 Berardino Parameterization

We apply the parameterization in terms of rate (Berardino et al., 2002), as outlined in Section 3.2. With this parameterization, the number of parameters is greater than the number of data such that $m_G > n_G$. Consequently, SVD yields a locally oscillatory solution (Figure 5.10). For the same reason, the variance of unit weight σ^2 cannot be calculated from equation (3.45). Instead, we interpret the null residuals as a perfect fit and set the misfit $\sigma_0 = 0$.

In addition, we apply first-order Tikhonov regularization to favor a constant-rate solution found using the method of Berardino et al. (2002) (Figure 5.11). We experiment with several values of smoothing parameters to find the solution to the weighted least-squares problem shown in Figure 5.11. We choose the regularization parameter $\beta = 0.0010$ based on the L-shaped curve of the norm of the residuals plotted as a function of the norm of the parameter vector to balance the trade-off between fitting the data and reducing the roughness. Comparing the enlarged sections of Figures 5.10 and 5.11, we see that the Tikhonov regularization mitigates the artifactual oscillations during the summers between 1999 and 2001. The sharp increase in rate beginning in summer 2001 remains apparent in Figure 5.11.

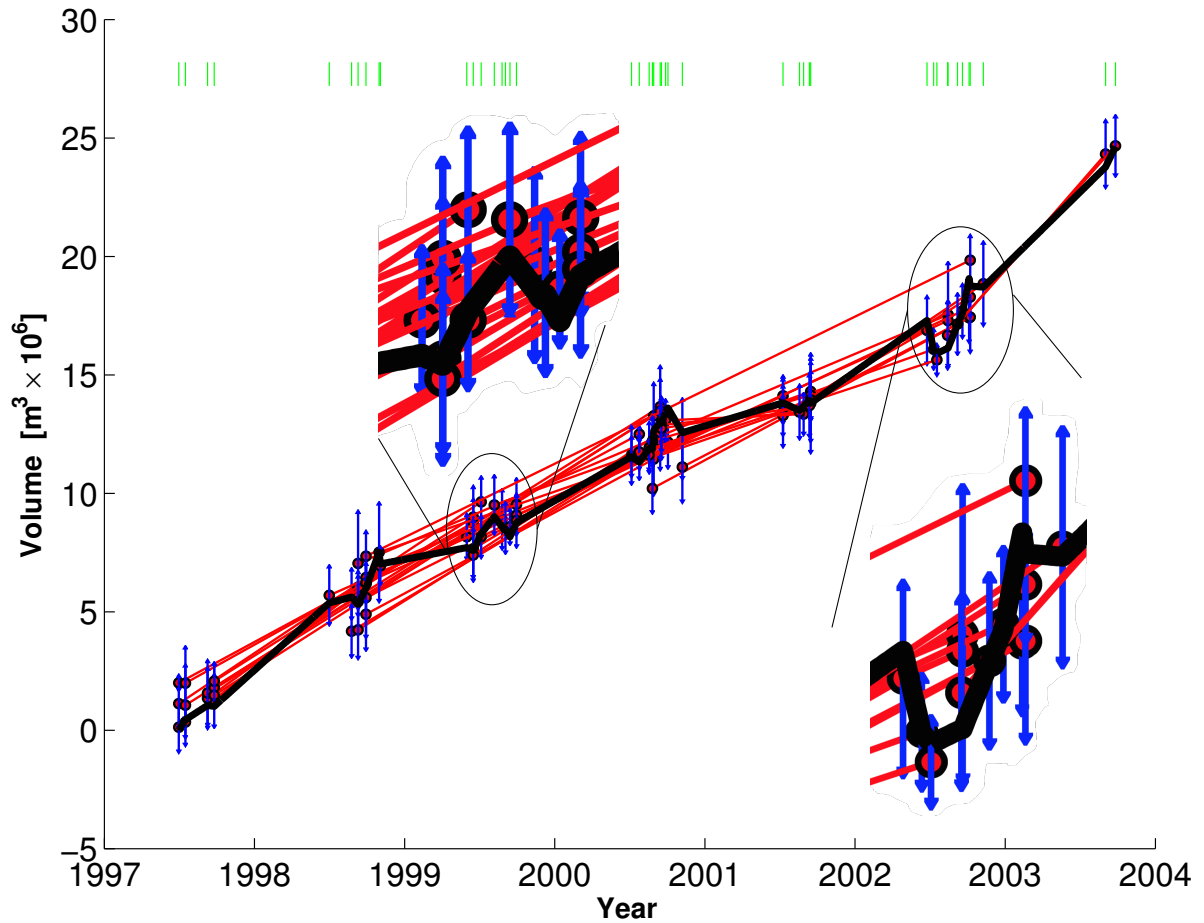


Figure 5.10: Volume increase as a function of time as estimated by temporal adjustment using the method of rates parameterized in terms of 44 velocity parameters as developed by Bernardino et al. (2002). Enlarged portions show the local oscillatory nature of the SVD minimum-length solution. Plotting conventions as in previous figure.

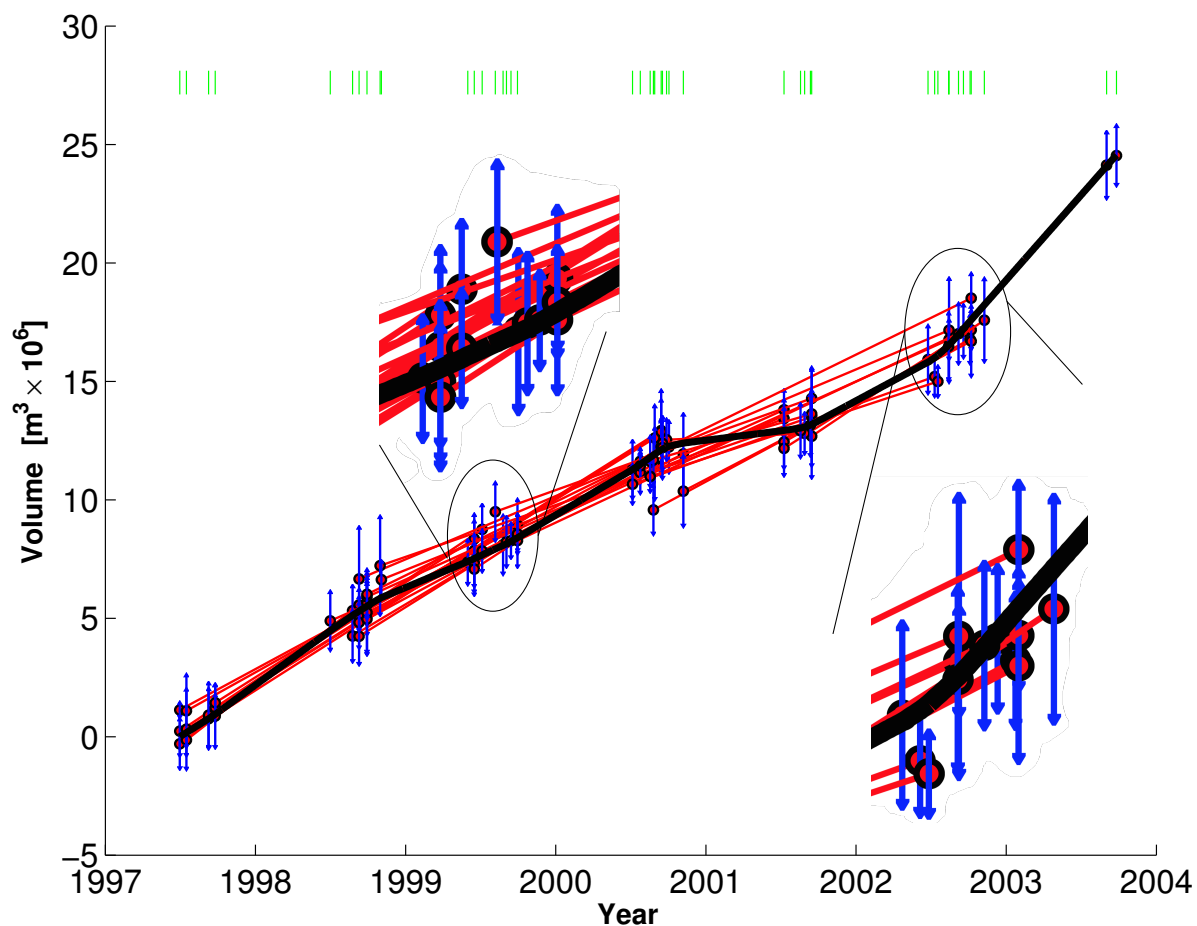


Figure 5.11: Volume increase as a function of time as estimated by temporal adjustment using the method of rates parameterized in terms of 44 velocity parameters as developed by Berardino et al. (2002) with first-order Tikhonov regularization to flatten the solution. We choose the regularization parameter $\beta = 0.0010$ based on an L-curve plot of the norm of the residuals against the norm of the parameter vector (e.g., Aster et al., 2013). Plotting conventions as in previous figure.

5.7 Exponential Decay Parameterization

We parameterize the time dependence as an exponentially decaying rate via equation (3.19). This formulation is compatible with viscoelastic relaxation, as suggested by previous studies of Okmok volcano (e.g., Fournier et al., 2009; Masterlark et al., 2010, 2016). We set t_0 at May 23, 1997, the end of the 1997 eruption. To estimate the best-fitting characteristic time constant $\tau_m \doteq 6$ years, we use nonlinear optimization via an “interior point” algorithm (e.g., Byrd et al., 2000) implemented in MATLAB (2014). This exponential model produces a slightly better fit ($\sigma_0 = 0.9455 \text{ m}^3$, Figure 5.12) than the single-segment (constant-rate) model.

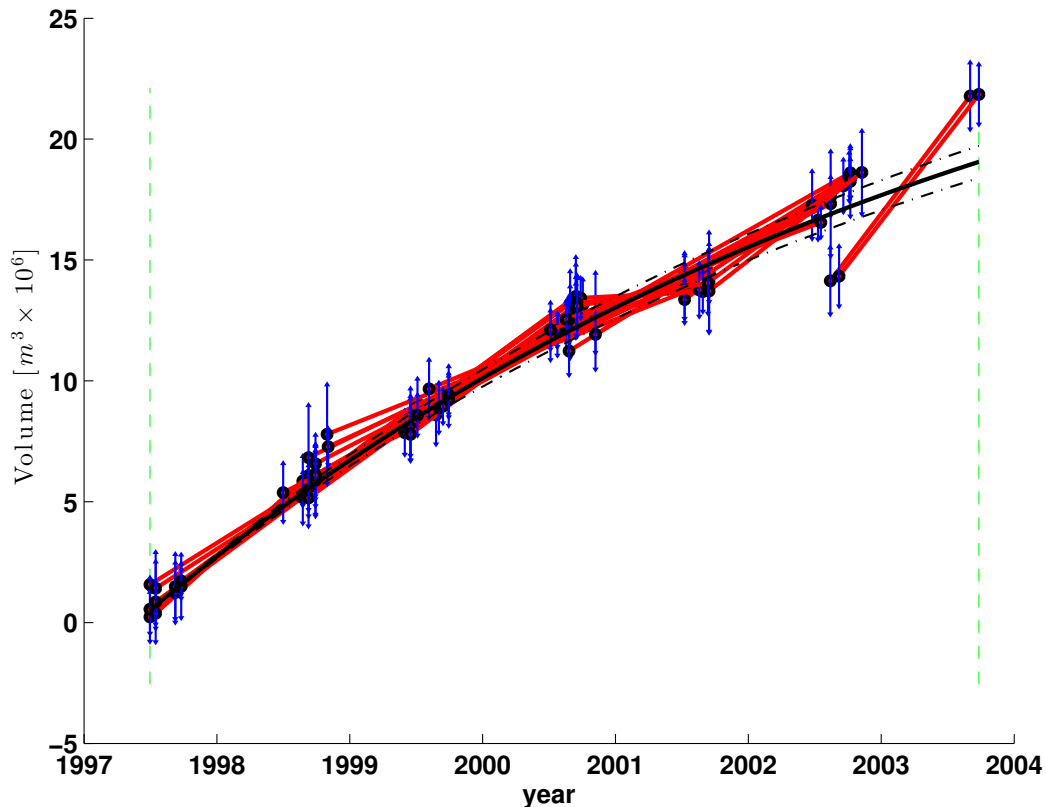


Figure 5.12: Volume increase as a function of time as estimated by temporal adjustment using the parametrization in terms of an exponentially decaying rate. The characteristic time scale is $\tau = 6.5$ years and reference time epoch at May 23, 1997. Misfit $\sigma_0 = 0.9455 \text{ m}^3$. Plotting conventions as in previous figure.

5.8 Modified Exponential Parameterization

In the GPS time series, Fournier et al. (2009) observe a rapid pulse of inflation beginning in the summer of 2002 (specifically stations OKCD and OKCE) (their Figure 6, our Figure 5.13) which is not consistent with the previous exponential trend. To account for it, we modify the exponential parameterization by adding a secular rate for the interval from June 21, 2002 to September 26, 2003, the last epoch in the time series. We define this interval by letting $t = t_{s1}$ and $t = t_{s2}$, corresponding to the beginning and end of the time span, respectively. The results of nonlinear optimization for an exponentially decaying rate until June 21, 2002 indicate a new best-fitting characteristic time scale of $\tau_m \doteq 5$ years. Extending equation (3.19), we choose a temporal function such that

$$\mathbf{m}f_{mexp}(t_i) = \begin{cases} m_1 \left(1 - \exp\left(-\frac{t_i - t_0}{\tau_m}\right)\right) & \text{if } t_i < t_{s1} \\ m_2(t_i - t_{s1}) & \text{if } t_{s1} \leq t_i \leq t_{s2} \\ 0 & \text{otherwise} \end{cases} \quad (5.2)$$

where the design matrix \mathbf{G} has three columns corresponding to the three elements in the parameter vector \mathbf{m} . This modification improves the fit to $\sigma_0 = 0.5685 \text{ m}^3$ (Figure 5.14).

To determine if the modification is justified, we perform an F test on the exponential decay and the modified exponential model (e.g., Wackerly et al., 2007). The null hypothesis states that the two sets of weighted residual values of displacement have equal variance. We find $F = 13.67$. Since the critical value of the F statistic for a significance level of $\alpha = 0.05$ and degrees of freedom $\nu_1 = n - 1 = 43$ and $\nu_2 = n - 3 = 41$ is $F_{\alpha, \nu_1, \nu_2} = 1.67$, the null hypothesis is rejected with 95% confidence. We conclude that the additional complexity of the modified exponential model is justified.

Next, we compare the modified exponential model with the 5-segment piecewise-linear parameterization. We know that the misfit of the 5-segment piecewise-linear model is less

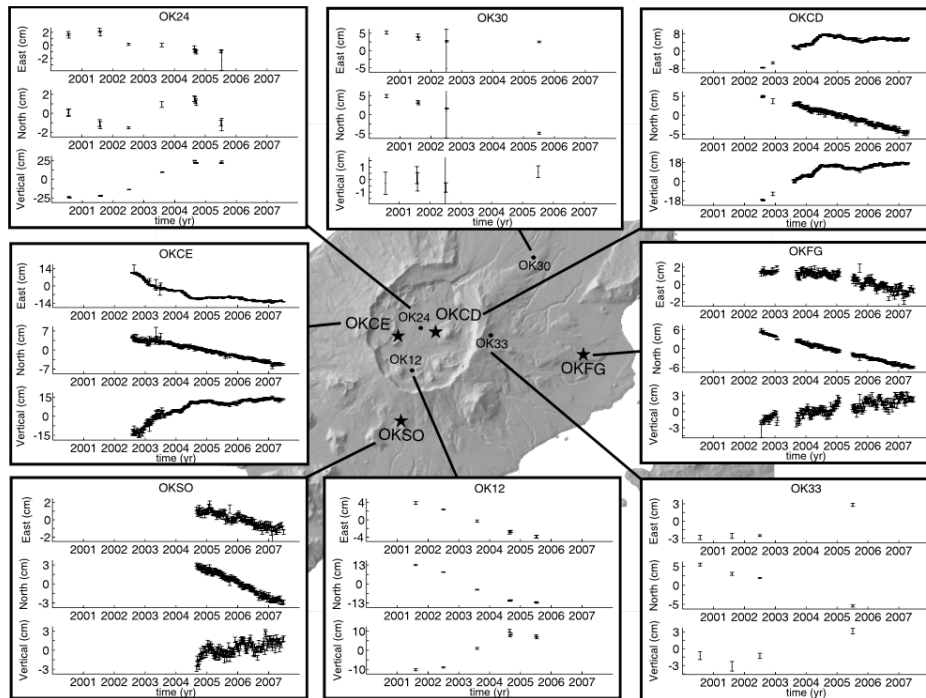


Figure 5.13: “Examples of time series from select sites are shown along with the site locations on the volcano. The two intracaldera CGPS sites, OKCD and OKCE, show inflation pulses that occurred in 2003 and 2004. Site OK24 recorded the largest vertical displacement, ~ 50 cm. The time series are shown in the ITRF and the ~ 2 cm/a southwestward regional velocity (Table 1) is apparent particularly at stations OKSO and OKFG.” figure and caption from Fournier et al. (2009, their Figure 6)

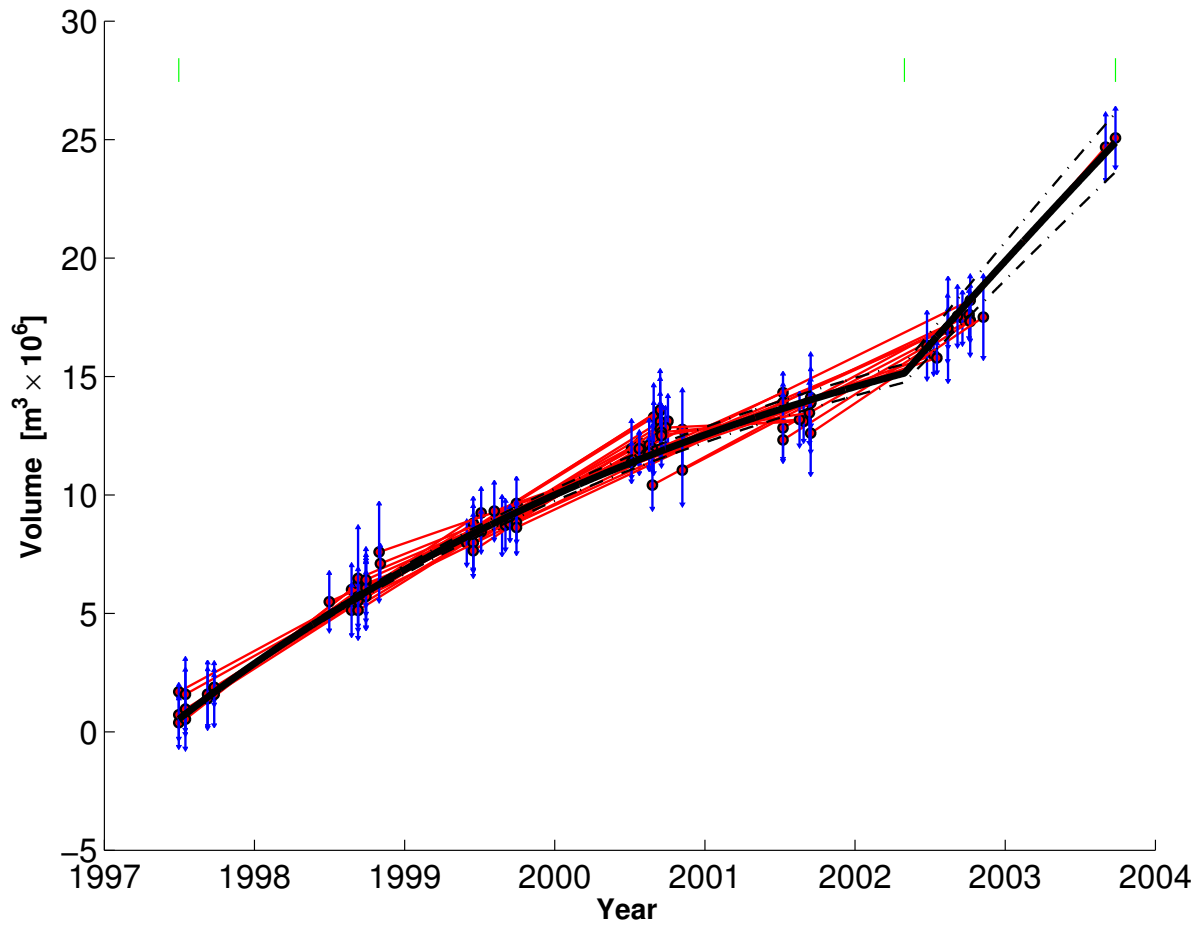


Figure 5.14: Volume increase as a function of time as estimated by temporal adjustment using the parametrization in terms of an exponentially decaying rate until June 21, 2002 and then a constant secular rate through the end of the data set at September 26, 2003. The characteristic time scale is $\tau_m = 4.9$ years. Misfit $\sigma_0 = 0.5685 \text{ m}^3$. Plotting conventions as in Figure 5.12.

than that of the modified exponential decay, but we must also consider their variances. We test the null hypothesis that the two sets of weighted residual values of displacement have equal variance. With a significance level of $\alpha = 0.05$ and degrees of freedom $\nu_1 = 42$ and $\nu_2 = 39$, the critical value of the F statistic is $F_{\alpha, \nu_1, \nu_2} = 1.69$. Since the calculated F value is 4.0211, and the null hypothesis is rejected with 95% confidence. Thus, we conclude that the 5-segment piecewise-linear parameterization provides a significantly better fit.

6 Discussion

Among the various parameterizations for Okmok, the empirical 5-segment piecewise linear model provides the best fit. The second-best fit is a modified exponential function. One interpretation suggests viscoelastic relaxation following the 1997 eruption (e.g., Jellinek and DePaolo, 2003). Another possibility is that the viscosity of magma flowing upward through a conduit into a shallow reservoir determines the characteristic time scale (e.g., Le Mével et al., 2015b). We examine these two mechanisms by applying temporal adjustment to pair-wise vertical displacements derived from the volume change estimates.

6.1 Estimating the Characteristic Time Scale at at Okmok Volcano

First, we convert the subset of pair-wise estimates of volume changes from Lu et al. (2005) to vertical displacement using the following relationship:

$$u_z = \frac{(1 - \nu_P)\Delta V}{\pi} \frac{d}{(R^2 + d^2)^{3/2}} \quad (6.1)$$

where ν_P represents Poisson's ratio, d is the depth to the center of the reservoir and R denotes the radial distance from the center of the reservoir to the point of interest (Segall, 2010). For simplicity, we consider only pairs with both acquisition dates before June 21, 2002. We consider a point located directly above the center of the reservoir. We take depth $d = 3.6$ km and $\nu_P = 0.25$ following Lu et al. (2005). We apply temporal adjustment to these values of vertical displacement \mathbf{u}_z parameterized in terms of exponentially decaying rate by equation (3.19). Results are shown in Figure 6.1.

To find the value of the characteristic time scale τ we perform a grid search. We define the misfit σ_0 according to equation 3.45. We constrain the characteristic time

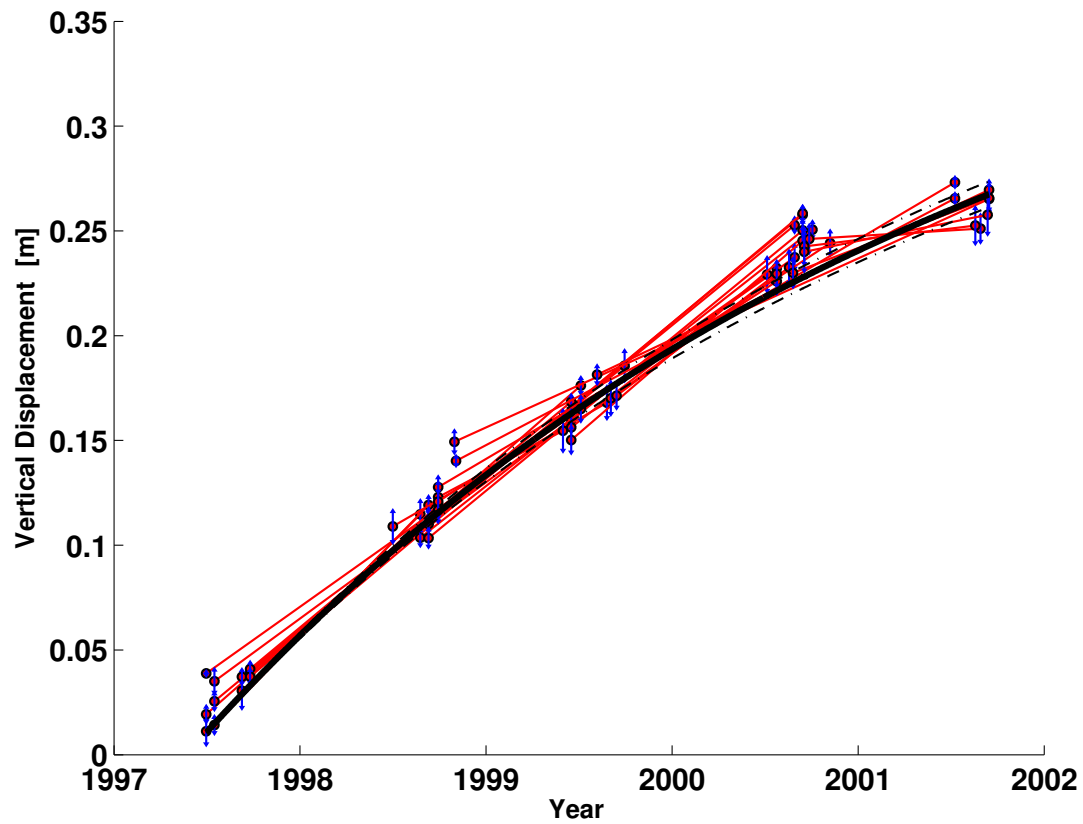


Figure 6.1: Vertical displacement of the magma chamber at a point directly above the center as a function of time as estimated by temporal adjustment using the parametrization in terms of an exponentially decaying rate until June 21, 2002. The characteristic time scale is $\tau = 4.1$ years. The acceptable range for τ according to our 95% confidence interval is 2–13 years. Misfit $\sigma_0 = 2.5077$. Plotting conventions as in previous figure.

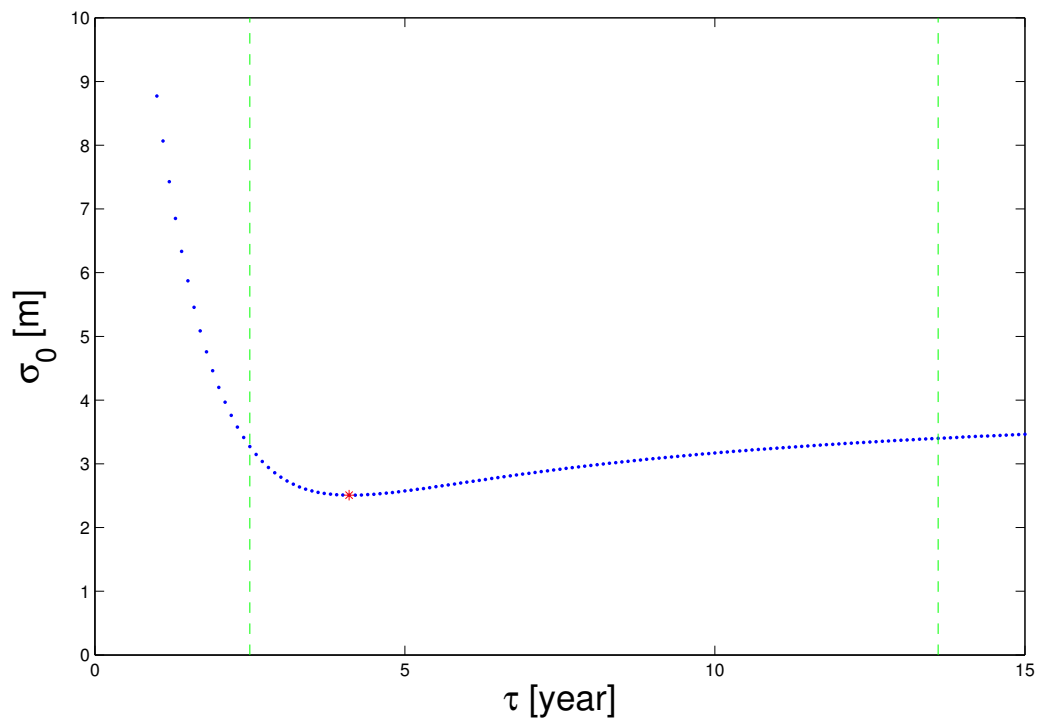


Figure 6.2: Misfit to the vertical displacement values in terms of σ_0 for parameter τ according to the one dimensional grid search applied to equation (3.19). The red star represents the best-fitting characteristic time scale $\tau = 4.1$ years, corresponding to a minimum misfit of $\sigma_0 = 2.5$. Green lines represent the 95% confidence interval.

scale to fall between 1 to 15 years, with increments of 0.1 year. After defining a value for τ during the grid search, the best-fitting value for the initial vertical displacement m_1 is found using temporal adjustment, as discussed in Chapter 3. We find that the lowest misfit, $\sigma_0 = 2.5077$, is found when $\tau = 4.1\text{yr}$ and $m_1 = (4.1 \pm 0.1) \times 10^{-1}$ m (see Figure 6.2).

6.2 Viscoelastic Relaxation of the Surrounding Country Rock

First, we interpret the characteristic time scale in terms of viscoelastic relaxation of the surrounding country rock (e.g., Masterlark et al., 2016). According to this hypothesis, we represent the characteristic time scale as (e.g., Segall, 2010; Masterlark et al., 2010)

$$\begin{aligned}\tau_{Maxwell} &= \frac{2\eta_c}{E} \\ &= \frac{\eta_c}{(G(1 + \nu_P))}\end{aligned}\tag{6.2}$$

where G represents the shear modulus and η_c represents the viscosity of the crust. In the case of a Poisson solid with $\nu_P = 1/4$, we have

$$\begin{aligned}\tau_{Maxwell} &= \frac{\eta_c}{G(5/4)} \\ &= \frac{4\eta_c}{5G}.\end{aligned}\tag{6.3}$$

To interpret this expression, we select geophysically reasonable values of G ranging from 1 GPa to 30 GPa (e.g., Feigl, 2002, and references therein). Combining the values of G with the 95% confidence interval for the characteristic time scale τ in Figure 6.3, we find corresponding values of η_c between 2×10^{17} Pa.s and 3×10^{19} Pa.s.

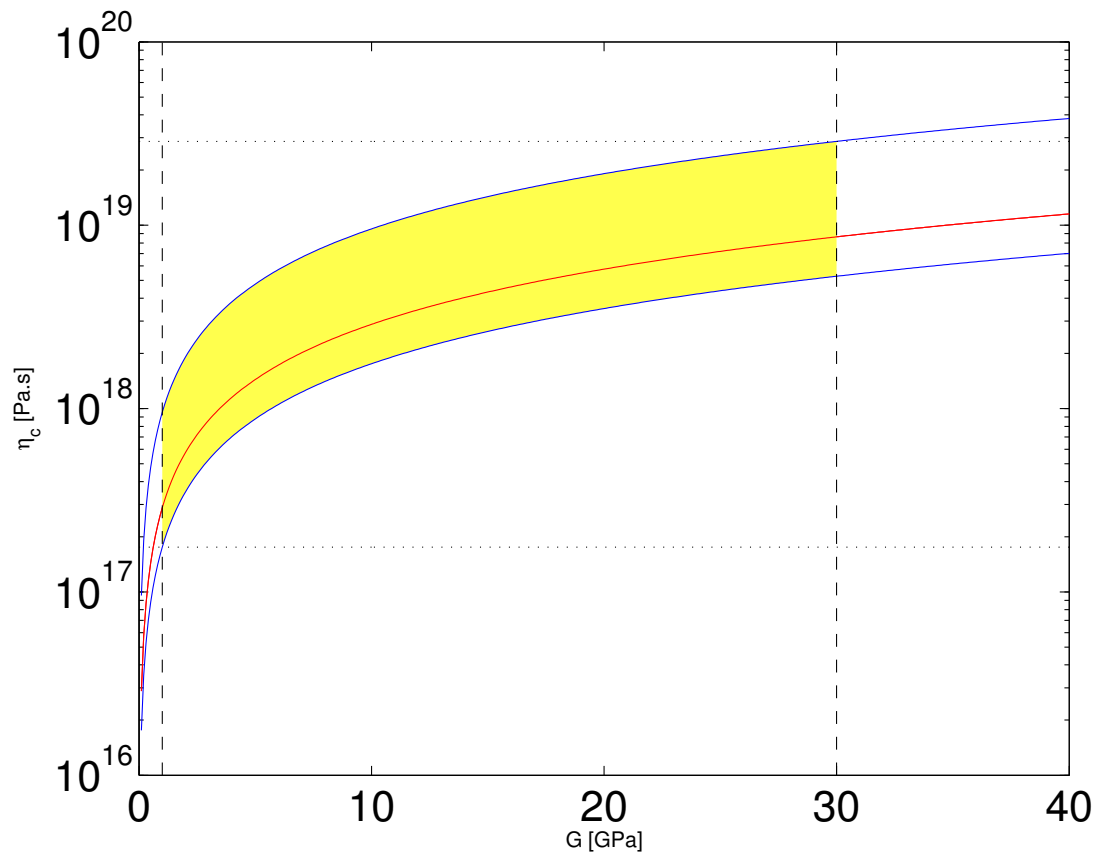


Figure 6.3: Range of acceptable values for η_c given $\tau_{Maxwell} = 4.1$ yr (red line) with a 95% confidence interval (blue lines). Yellow region indicates values of η_c that are compatible with geophysically reasonable values for the shear modulus G .

6.3 Viscous Magma Flow Upwards Through a Conduit

As a second hypothesis, we consider the mechanism proposed by Le Mével et al. (2015b). In this model, viscous magma flows upwards through a cylindrical conduit into a fluid-filled, spherical reservoir (see Figure 6.4). Assuming laminar flow in the lower crust, the volumetric flow rate is governed by the Hagen-Poiseuille law. In the case of Okmok Volcano, we assume a constant injection pressure ΔP_i is applied to the inlet of the conduit. Le Mével et al. (2016) solve the differential equation for reservoir pressure at the conduit outlet $\Delta P_o(t)$. The initial condition on the reservoir pressure at the conduit outlet is $\Delta P_o(t = 0) = 0$. The expression for the reservoir pressure at the conduit outlet ΔP_i is expressed as (Le Mével et al., 2016, their equation (3.9)):

$$\Delta P_o(t) = P \left(1 - \exp \left(-\frac{t}{\tau} \right) \right) \quad (6.4)$$

with

$$P = \Delta P_i + (\rho_r - \rho_m)gL_c \quad (6.5)$$

where ρ_r represents the density of crustal rocks, ρ_m represents the density of magma, g represents gravitational acceleration, and L_c denotes the length of the conduit. The characteristic time scale is represented as

$$\tau_{Poiseuille} = \frac{8\eta_m L_c a^3}{Ga_c^4} \quad (6.6)$$

where η_m represents the viscosity of the magma, a denotes the radius of the spherical reservoir, and a_c denote the radius of the cylindrical conduit. We set $a_c = 50$ m, $L_c = 2000$ m, and $a = 1000$ m following results from previous studies (e.g., Lu et al., 2005; Fournier et al., 2009; Haney, 2010; Masterlark et al., 2010; Le Mével et al., 2016).

We can use these equations to derive an expression for the vertical displacement of

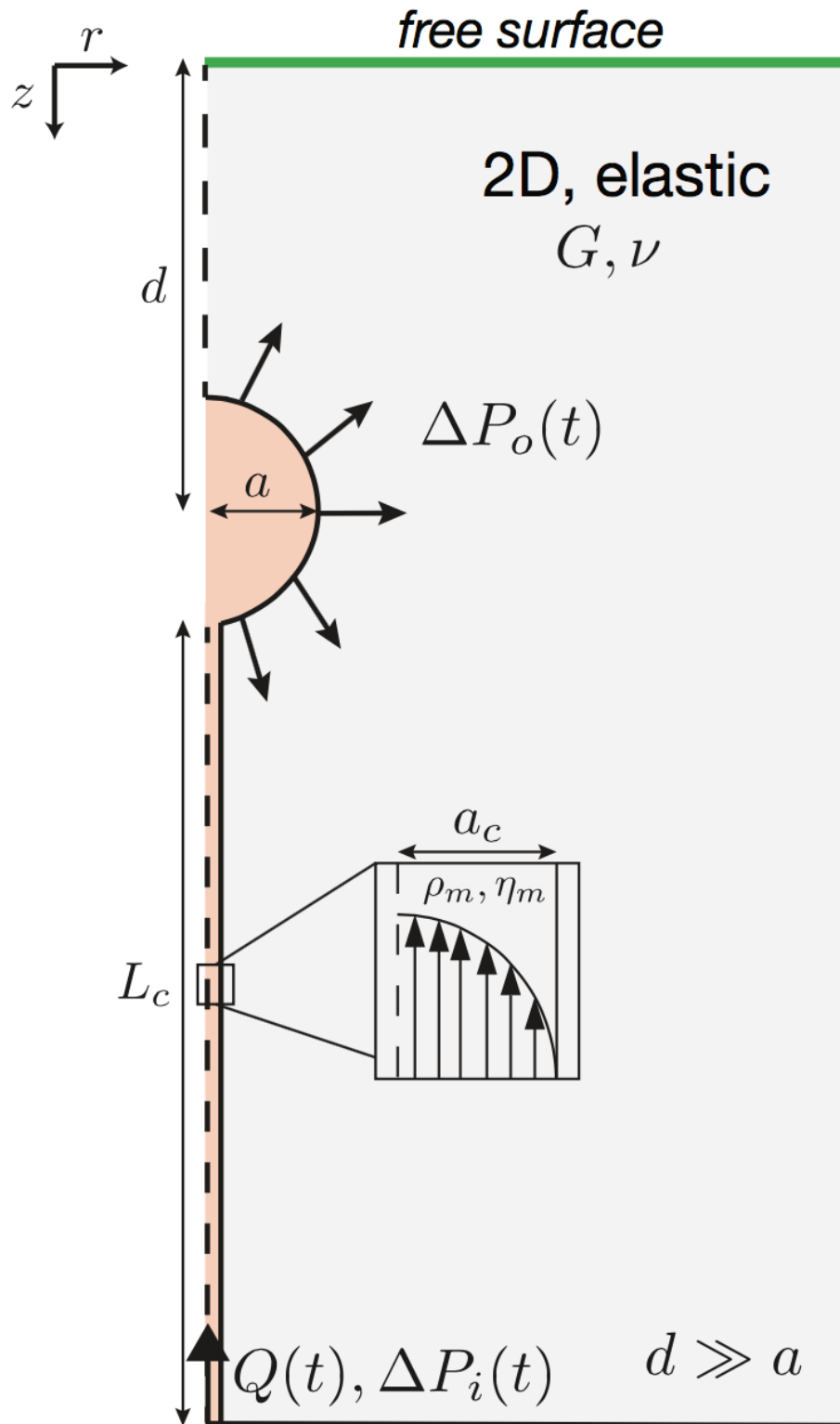


Figure 6.4: Panel (b) figure and caption from Le Mével et al. (2016, their Figure 6.3), “the new model of laminar flow into a magma-filled reservoir (analytic solution)”.

a particle at a point located directly above the top of the magma reservoir (Le Mével et al., 2016, their equation (3.14))

$$\begin{aligned} u_z(t) &= \frac{(1 - \nu_P)a^3}{Gd^2} \Delta P_o(t) \\ &= \frac{(1 - \nu_P)a^3}{Gd^2} (\Delta P_i + (\rho_r - \rho_m)gL_c) \left(1 - \exp\left(-\frac{t}{\tau}\right) \right) \end{aligned} \quad (6.7)$$

To interpret the estimated value of the characteristic time scale $\tau_{Poiseuille}$, we consider geophysically reasonable values of the shear modulus and compare them to values of η_m . The results are shown in Figure 6.5. The best-fitting characteristic time scale found in Section 6.1 corresponds to possible values of η_m between 2×10^{10} Pa.s and 5×10^{12} Pa.s.

Additionally, we consider our 95% confidence interval for $\tau_{Poiseuille}$ and geophysically reasonable values of the shear modulus to find compatible values of a_c . The results are shown in Figure 6.6. We find acceptable values of a_c ranging from 20–70 m, which agrees with our assumption of $a_c = 50$ m.

We also consider our 95% confidence interval for $\tau_{Poiseuille}$ with geophysically reasonable values of the conduit length L_c to find compatible values of the ratio between reservoir radius and conduit radius $\frac{a^3}{a_c^4}$. The results are shown in Figure 6.7. We see that for a range of L_c between 1000 m and 2000 m, we find a corresponding range for the ratio $\frac{a^3}{a_c^4}$ between $4 \times 10^4 \text{ m}^{-1}$ and 10^6 m^{-1} . Thus, a value of $a = 1000$ m and $a_c = 50$ m yields a ratio of $\frac{a^3}{a_c^4} = \frac{(1 \times 10^3 \text{ m})^3}{(5 \times 10^1 \text{ m})^4} = \frac{1 \times 10^9}{5 \times 10^4} \text{ m}^{-1} = 2 \times 10^4 \text{ m}^{-1}$.

Finally, we consider the 95% confidence interval for $\tau_{Poiseuille}$ and geophysically reasonable values of the shear modulus to find compatible values of L_c . The results are shown in Figure 6.8. We see that for a range of G between 1–30 GPa, we have a corresponding range of conduit length between 0.5–89 km. This suggests that while our assumption of $L_c = 2$ km lies within this range, we may also consider greater conduit lengths in future studies.

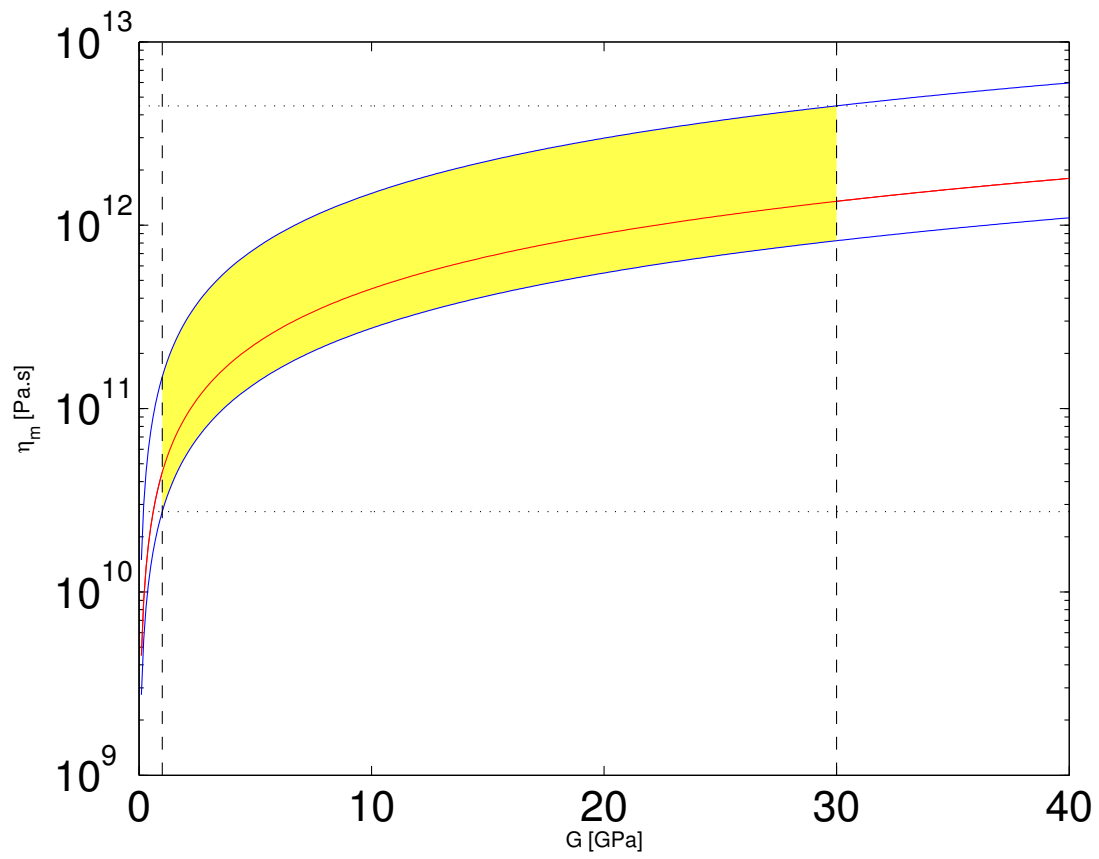


Figure 6.5: Range of acceptable values for η_m given $\tau_{Poiseuille} = 4.1$ yr (red line) with a 95% confidence interval (blue lines). Yellow region indicates values of η_m that are compatible with geophysically reasonable values for the shear modulus G .

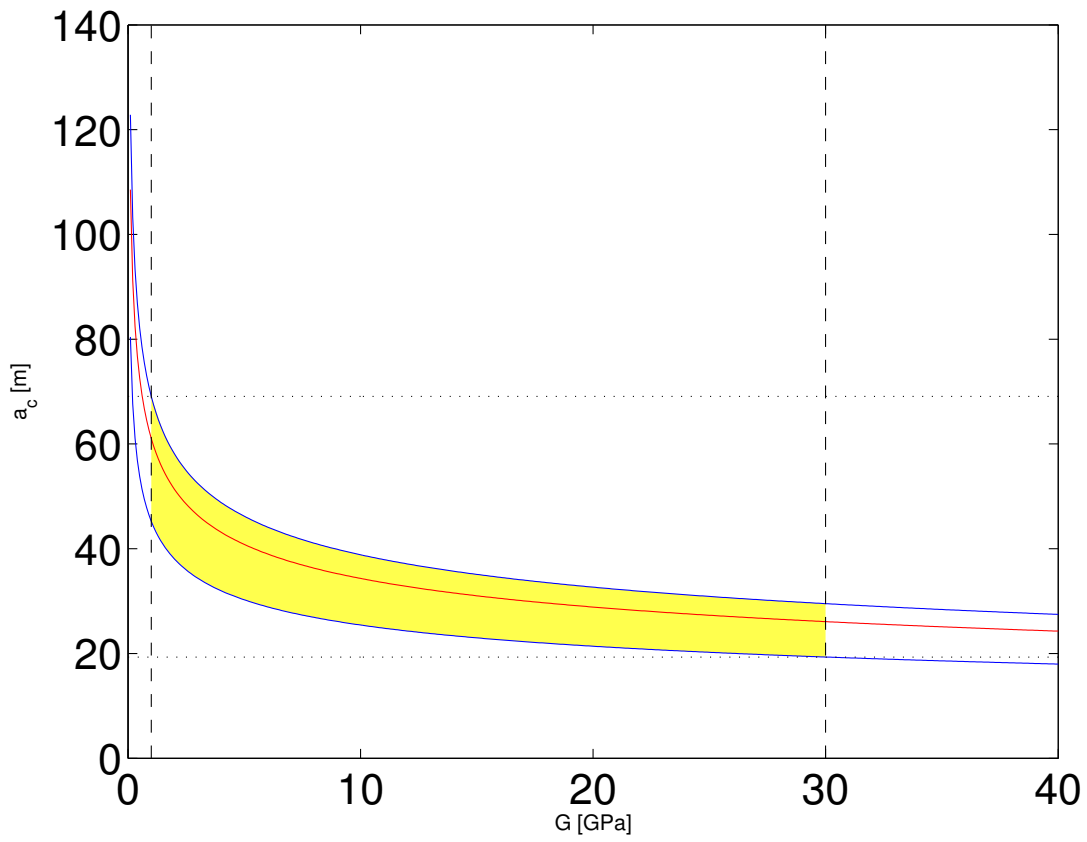


Figure 6.6: Range of acceptable values for a_c given $\tau_{Poiseuille} = 4.1$ yr (red line) with a 95% confidence interval (blue lines). Yellow region indicates values of a_c that are compatible with geophysically reasonable values for the shear modulus G .

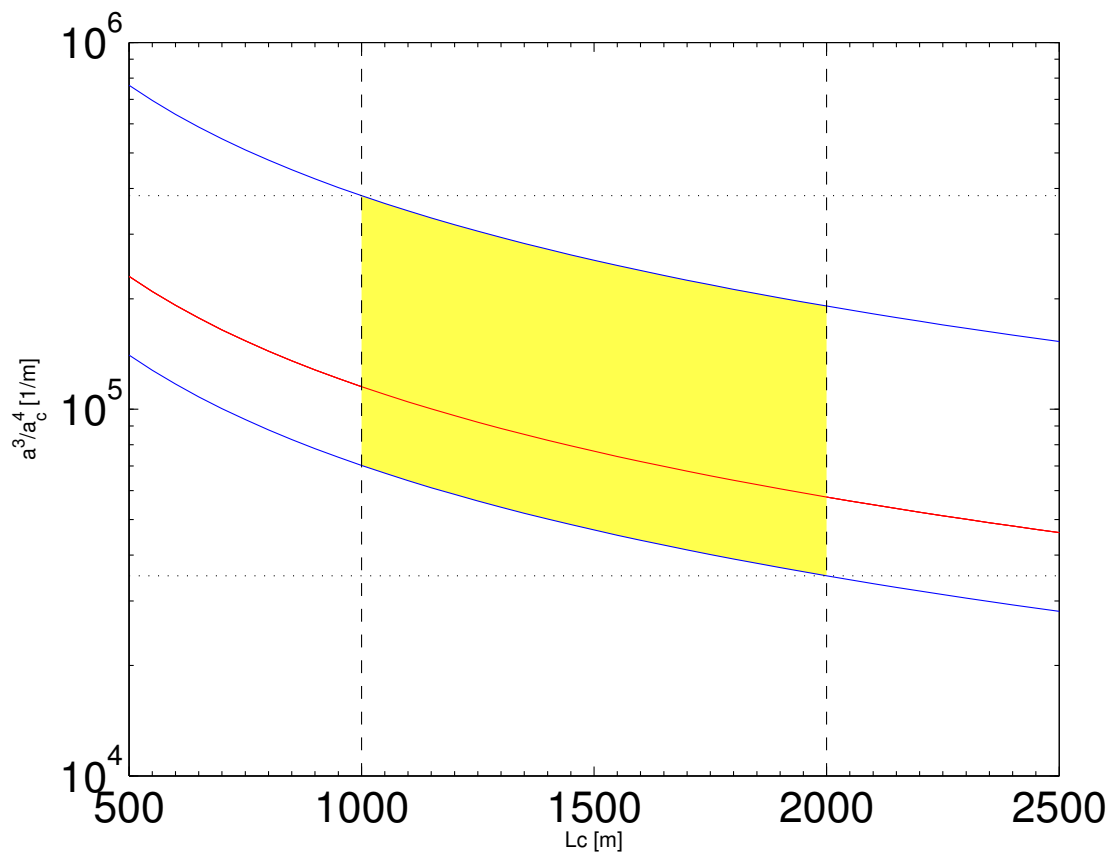


Figure 6.7: Range of acceptable values for $\frac{a^3}{a_c^4}$ given $\tau_{Poiseuille} = 4.1$ yr (red line) with a 95% confidence interval (blue lines). Yellow region indicates values of $\frac{a^3}{a_c^4}$ that are compatible with geophysically reasonable values for conduit length L_c .

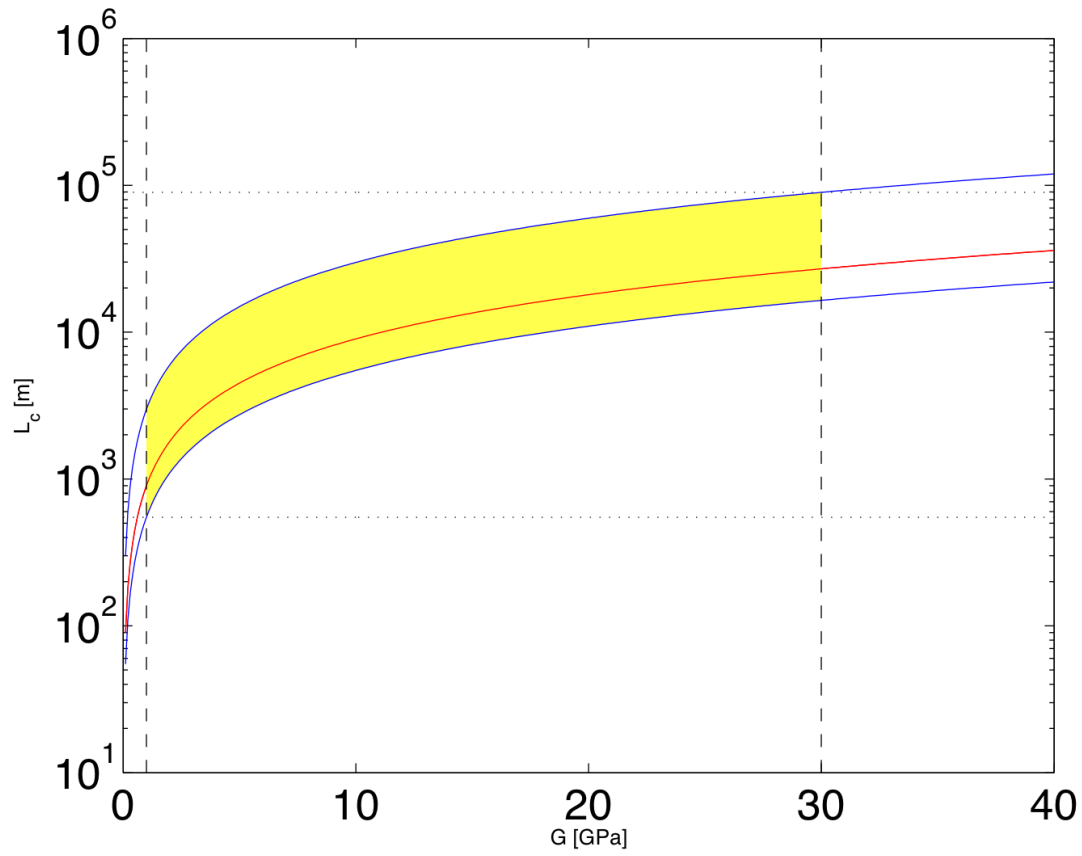


Figure 6.8: Range of acceptable values for L_c given $\tau_{Poiseuille} = 4.1$ yr (red line) with a 95% confidence interval (blue lines). Yellow region indicates values of L_c that are compatible with geophysically reasonable values for the shear modulus G .

6.4 Secondary Pulses?

Between June of 2002 and September 2003, the estimated rate of volumetric increase is $6.2 \pm 0.6 \times 10^6 \text{ m}^3/\text{yr}$. This result is consistent with the suggestion of a “pulse of rapid inflation” from “summer 2002 to late 2003” (Fournier et al., 2009; Biggs et al., 2010). If viscoelastic relaxation also occurred in the years following this pulse, then we would expect slower inflation and/or deflation in later years (e.g., Masterlark et al., 2016). In this case, the characteristic time scale would be of the same order of magnitude as found earlier, i.e. ~ 4 years (e.g., Hetland and Hager, 2005). Alternatively, Fournier (2008) suggests degassing to explain the slowing rate of inflation that began in 2004.

7 Conclusions

We have shown that graph theory is useful for analyzing pair-wise InSAR data in the temporal domain. In particular, the normalized edge Laplacian matrix calculated from the edge-vertex incidence matrix of the graph of the data set represents its correlation.

This formulation also leads to the covariance matrix of the epoch-wise measurements to calculate their relative uncertainties. For example, the Okmok data set shows greater uncertainty for single-epoch, individual SAR images acquired during the winter season than for those in the summer. Although mathematically straightforward, this derivation has not been previously applied to InSAR data.

If the number of distinct trees or components is greater than one, then a piecewise linear parameterization in terms of rates, as proposed by Berardino et al. (2002), leads to a locally oscillatory solution. To mitigate this issue, we use first-order Tikhonov regularization.

Using graph theory, we have derived a result for the pair-wise data covariance matrix that agrees with previous formulae while providing useful insight into the graphical structure of the data. Moreover, the formulation is concise and independent of the choice of model.

The formulation in terms of incidence graphs also applies to any quantity derived from pair-wise differences. For example, plots of orbital separation B_{\perp} as a function of time are calculated with respect to a “virtual” reference orbit with a constraint of zero mean, as shown in Figure 5.6 (e.g., Fialko et al., 2002). Similarly, one could apply temporal adjustment to individual, co-located pixels in a time series of interferograms or even their decomposition into wavelets (e.g., Jolivet et al., 2015).

This method has also been applied to analyze pair-wise volume changes in a geothermal field at Brady’s Hot Springs, Nevada (Ali et al., 2016). As a co-author, I contributed to this study by analyzing the time series of volume changes estimated from InSAR data between 2004 and 2014. An 8-segment piecewise linear parameterization was applied to

the time series. The results were compared to flow rates in production wells. This comparison suggests a correlation between the volume changes estimated from the InSAR time series and the production in shallow wells.

Appendix A

Mathematical Notation

Table of mathematical symbols.

Symbol	Meaning
\mathbf{A}^\dagger	pseudoinverse of \mathbf{A}
\mathbf{A}^\top	transpose of \mathbf{A}
\mathbf{A}^{-1}	inverse of \mathbf{A}
\mathbf{B}	pair-rate incidence matrix
B_\perp	orbital separation, perpendicular baseline
\mathbf{C}	constraint matrix with k rows
c	number of pair-wise combinations as defined in Feigl and Thurber (2009)
$corr$	correlation coefficient
\mathbf{D}	n -by- n diagonal matrix of degrees in graph of data set
d	depth to center of reservoir in Mogi model (Segall, 2010)
\mathbf{d}	n -by-1 data vector
\mathbf{d}_{con}	k -by-1 vector of data constraints
\mathbf{d}_{mod}	vector of modeled displacement
\mathbf{d}_{obs}	n -by-1 vector of observed data
$diag$	operator transforming a vector into a diagonal matrix
e_i	i^{th} edge
E	Young's modulus
F_{α, ν_1, ν_2}	critical value for F test
$f_{obj}(\mathbf{d}; \mathbf{m})$	objective function for weighted least-squares
$f(t)$	temporal function
G	shear modulus
g	gravitational acceleration
\mathbf{G}	n -by- m design matrix
$\mathbf{G}_{n \times (m-1)}^{[B]}$	Berardino et al. (2002) design matrix
\mathbf{K}	n -by- n edge-version of the Laplacian
k	number of components of a disconnected graph
\mathbf{L}	normalized edge-version of the Laplacian
\mathbf{L}_ρ	correlation matrix of epoch-wise measurements
\mathbf{m}	m -by-1 vector of model parameters
m	number of elements in parameter vector
$\tilde{\mathbf{m}}$	estimated model parameter vector
m_G	number of columns of \mathbf{G}
n	number of elements in data vector
n_G	number of rows of \mathbf{G}

n -by- m	matrix having n rows and m columns
ΔP_o	reservoir pressure at conduit outlet (Le Mével et al., 2016)
ΔP_i	injection pressure at conduit inlet (Le Mével et al., 2016)
\mathbf{Q}	n -by- q edge-vertex incidence matrix
q	number of epochs as defined in Feigl and Thurber (2009)
$q_{i,j}$	element in the i^{th} row and j^{th} column of \mathbf{Q}
\mathbf{r}	vector of residuals
$\text{rank}(\mathbf{Q})$	rank of the incidence matrix
R	radial distance from center of reservoir to point of interest in Mogi model (Segall, 2010)
RMSE	root-mean-squared error
\mathbf{S}	n -by- n diagonal matrix of sample standard deviation of pair-wise measurement errors
SVD	singular value decomposition
\mathbf{T}	m -by- m diagonal matrix of time intervals
\mathbf{t}	vector of unique epochs in chronological order
t_0	reference epoch for exponentially decaying rate parameterization
t_i	the i^{th} epoch, or the i^{th} element of \mathbf{t}
t_q	predefined reference epoch
t_{s1}	lower bound epoch for modified exponentially decaying rate parameterization
t_{s2}	upper bound epoch for modified exponentially decaying rate parameterization
$T_{\nu, \frac{\alpha}{2}}$	critical value for two-tailed Student t-test
u_z	vertical displacement derived from Mogi source model (Segall, 2010)
\mathbf{v}	vector/set of rate parameters having $(m - 1)$ elements
v_i	i^{th} element of V or vertex
\mathbf{W}	matrix quantifying the solution roughness in Tikhonov regularization
α	significance level
β	Tikhonov regularization parameter
Δ	edge-vertex matrix of path
$\delta_{i,j}$	the $(i, j)^{\text{th}}$ element of the Kronecker delta
ϵ	strain
η	viscosity of material
η_c	viscosity of crust
η_i	number of epochs in the i^{th} component
η_m	viscosity of magma (Le Mével et al., 2016)
μ	rank deficiency of an underdetermined system
ν	degrees of freedom
ν_1	numerator degrees of freedom (F test)
ν_2	denominator degrees of freedom (F test)
ν_P	Poisson's ratio
ρ_m	density of magma

ρ_r	density of crust
ρ	vector of range
$\rho(t_i)$	range at epoch t_i
σ_s	stress
σ_{s0}	initial stress
$\Sigma_{\mathbf{d}}$	covariance matrix of pair-wise data
$\Sigma_{\mathbf{m}}$	scaled covariance matrix of model parameters
$\sigma_{\mathbf{m}}$	estimated standard deviation of model parameters
σ_{ρ}	vector of relative uncertainties of epoch-wise measurements
Σ'_{ρ}	covariance matrix of relative epoch-wise measurements
σ_0^2	fit, or variance of unit weight, as calculated from weighted residual scatter
σ_r^2	mean of the RMSEs of the Okmok data set
τ_m	characteristic time constant for exponential parameterizations
χ^2	chi-squared test statistic

List of alphabetically sorted mathematical symbols used throughout the text with English alphabet letters appearing before Greek alphabet letters.

Appendix B

Revised Data Table from Lu et al. (2005)

(see next page for long table)

Okmok dataset from Lu et al. (2005) with a priori uncertainties of pair-wise measurements.

ID	Orbit	Year	Month	Day	Orbit	Year	Month	Day	Track	Bn_in_m	dV_m^3	RMSE, mm	dV/dt (m^3)/yr	σ (m^3)/yr
1	106773	1992	10	31	112284	1993	11	20	115	13	7.65E+06	12.7	7.26E+06	2.42E+06
4	110738	1993	8	4	121603	1995	9	1	72	-154	3.55E+06	9.7	1.71E+06	9.39E+05
5	110738	1993	8	4	207441	1996	9	27	72	-136	2.46E+06	8.2	7.81E+05	5.23E+05
6	110781	1993	8	7	122147	1995	10	9	115	304	3.71E+06	8	1.71E+06	7.40E+05
7	111239	1993	9	8	122104	1995	10	6	72	-230	2.99E+06	9.2	1.44E+06	8.90E+05
8	111282	1993	9	11	122147	1995	10	9	115	-97	2.97E+06	10	1.43E+06	9.68E+05
9	111740	1993	10	13	122104	1995	10	6	72	-24	2.33E+06	8.2	1.18E+06	8.32E+05
10	111740	1993	10	13	207441	1996	9	27	72	-339	2.32E+06	10.1	7.85E+05	6.87E+05
11	111783	1993	10	16	122147	1995	10	9	115	-72	2.08E+06	7.8	1.05E+06	7.92E+05
12	112012	1993	11	1	122376	1995	10	25	344	71	1.95E+06	5.4	9.84E+05	5.48E+05
13	112012	1993	11	1	202703	1995	10	26	344	154	1.65E+06	6	8.32E+05	6.08E+05
14	121603	1995	9	1	207441	1996	9	27	72	18	-1.34E+06	4.5	-1.25E+06	8.44E+05
21	210719	1997	5	8	217733	1998	9	10	344	167	7.11E+06	5.1	5.30E+06	7.64E+05
22	211492	1997	7	1	217504	1998	8	25	115	236	5.62E+06	7.2	4.88E+06	1.26E+06
23	211492	1997	7	1	222013	1999	7	6	115	-119	8.52E+06	7.1	4.23E+06	7.09E+05
24	211492	1997	7	1	227524	2000	7	25	115	-72	1.05E+07	2	3.42E+06	1.31E+05
25	211721	1997	7	17	217733	1998	9	10	344	69	5.70E+06	4.4	4.95E+06	7.69E+05
26	211721	1997	7	17	221741	1999	6	17	344	48	6.77E+06	10.5	3.53E+06	1.10E+06
27	211721	1997	7	17	228254	2000	9	14	344	-41	1.26E+07	11.7	3.98E+06	7.44E+05
28	212494	1997	9	9	218005	1998	9	29	115	190	4.82E+06	8.7	4.57E+06	1.66E+06
29	212494	1997	9	9	228025	2000	8	29	115	-80	1.17E+07	9.4	3.94E+06	6.36E+05
30	212723	1997	9	25	217733	1998	9	10	344	92	3.88E+06	3.7	4.05E+06	7.76E+05
31	212723	1997	9	25	221741	1999	6	17	344	-25	6.92E+06	5.1	4.01E+06	5.94E+05
32	212723	1997	9	25	228254	2000	9	14	344	-18	1.20E+07	9.2	4.04E+06	6.22E+05
33	216731	1998	7	2	222743	1999	8	26	344	-251	3.21E+06	8.5	2.79E+06	1.48E+06
34	217504	1998	8	25	228526	2000	10	3	115	-11	7.98E+06	7.4	3.79E+06	7.06E+05
35	217733	1998	9	10	223244	1999	9	30	344	295	4.10E+06	7.4	3.89E+06	1.41E+06
36	217733	1998	9	10	228254	2000	9	14	344	-110	7.97E+06	8.2	3.96E+06	8.19E+05
37	217733	1998	9	10	238274	2002	8	15	344	216	1.05E+07	15.2	2.56E+06	7.78E+05
38	218005	1998	9	29	221512	1999	6	1	115	77	1.72E+06	6.4	2.67E+06	1.92E+06
39	218005	1998	9	29	228025	2000	8	29	115	-270	6.55E+06	10.4	3.42E+06	1.09E+06
40	218005	1998	9	29	229027	2000	11	7	115	-147	6.70E+06	11.6	3.18E+06	1.11E+06
41	218005	1998	9	29	232534	2001	7	10	115	120	7.90E+06	5.6	2.84E+06	4.05E+05
42	218005	1998	9	29	239047	2002	10	8	115	56	1.25E+07	7.1	3.11E+06	3.55E+05
43	218463	1998	10	31	233493	2001	9	15	72	-11	6.29E+06	14.4	2.19E+06	1.01E+06
44	218506	1998	11	3	232534	2001	7	10	115	-90	6.80E+06	5.3	2.54E+06	3.97E+05
46	221741	1999	6	17	227252	2000	7	6	344	-217	3.96E+06	8.3	3.76E+06	1.58E+06
47	221741	1999	6	17	228254	2000	9	14	344	7	5.16E+06	7.5	4.15E+06	1.21E+06
48	222013	1999	7	6	227524	2000	7	25	115	47	3.31E+06	5.9	3.14E+06	1.13E+06
49	222471	1999	8	7	233493	2001	9	15	72	-283	4.79E+06	8.4	2.27E+06	8.01E+05
50	222850	1999	9	3	227860	2000	8	18	451	108	3.39E+06	7.2	3.54E+06	1.51E+06
51	223015	1999	9	14	227524	2000	7	25	115	274	3.16E+06	4.9	3.67E+06	1.14E+06
52	223244	1999	9	30	238274	2002	8	15	344	-79	8.21E+06	5.6	2.86E+06	3.92E+05
53	223244	1999	9	30	238775	2002	9	19	344	33	8.84E+06	7.6	2.98E+06	5.14E+05
55	227252	2000	7	6	237773	2002	7	11	344	-187	4.54E+06	5.6	2.26E+06	5.59E+05
56	227982	2000	8	26	233493	2001	9	15	72	402	1.94E+06	6.8	1.84E+06	1.30E+06
57	227982	2000	8	26	239004	2002	10	5	72	75	7.20E+06	7	3.41E+06	6.67E+05
58	229027	2000	11	7	239047	2002	10	8	115	203	6.33E+06	10.2	3.30E+06	1.07E+06
59	232534	2001	7	10	237544	2002	6	25	115	-183	3.48E+06	9.8	3.63E+06	2.05E+06
60	232534	2001	7	10	239047	2002	10	8	115	-64	5.00E+06	5.6	4.01E+06	9.03E+05
61	233493	2001	9	15	239505	2002	11	9	72	93	4.90E+06	12.1	4.26E+06	2.11E+06
65	227860	2000	8	18	237880	2002	7	19	451	8	4.01E+06	4.3	2.09E+06	4.51E+05
66	122147	1995	10	9	212494	1997	9	9	115	8	-4.82E+07	9.8	-2.51E+07	1.03E+06
67	122147	1995	10	9	212494	1997	9	9	115	8	-4.73E+07	8.7	-2.47E+07	9.12E+05
68	325570	2000	9	27	330372	2001	8	29	800	-118	2.68E+05	5.8	2.91E+05	1.27E+06
70	325420	2000	9	17	330222	2001	8	19	900	362	5.39E+05	7.7	5.86E+05	1.68E+06
71	325420	2000	9	17	330565	2001	9	12	900	350	9.55E+05	8.9	9.69E+05	1.82E+06
74	403682	1992	10	13	435314	1998	7	26	777	240	-3.39E+07	10.2	-5.86E+06	3.55E+05

Figure B.1: Table showing the Okmok dataset from citetlu2005 with *a priori* uncertainties of pair-wise measurements. “Dates are image acquisition times. Orbit numbers include the satellite ID (1, ERS1; 2, ERS2; 3, RADARSAT1; and 4, JERS1) and orbit on which the images were acquired. The same track number applies to both images in an InSAR pair. B_n is the perpendicular component of the baseline with respect to the SAR look angle. dV is the volume change of the source of the best fitting model in the case that the model source in three dimensions was fixed. RMSE is the root-mean-square error between the observed and modeled interferograms. Interferograms 66 and 67 are from the same, original interferogram. Phase values in the original interferogram, however, are discontinuous between two major patches which are represented by interferograms 66 and 67, respectively. So, interferograms 66 and 67 are treated as two different images.” (Lu et al., 2005). In our analysis, we abridge the dataset to include only pairs with acquisitions after the end of the 1997 eruption (May 25, 1997). The volume change rate per pair in column 14 is found by dividing the volumetric estimate by the corresponding time interval. The uncertainty of volume change rate in column 15 is estimated by scaling the individual RMSE values by their mean $\sigma_r = 4.98$ [mm].

Bibliography

- Agram P. S., Simons M. (2015) A noise model for InSAR time series. *Journal of Geophysical Research: Solid Earth* DOI 10.1002/2014JB011271
- Ali S., Akerley J., Baluyut E., Cardiff M., Davatzes N., Feigl K., Foxall W., Fratta D., Mellors R., Spielman P., et al. (2016) Time-series analysis of surface deformation at brady hot springs geothermal field (nevada) using interferometric synthetic aperture radar. *Geothermics* 61:114–120
- Aster R. C., Borchers B., Thurber C. H. (2013) *Parameter Estimation and Inverse Problems*, 2nd edn. Academic Press, 360 pp.
- Beauducel F., Briole P., Froger J.-L. (2000) Volcano-wide fringes in ERS synthetic aperture radar interferograms of Etna (1992–1998): Deformation or tropospheric effect? *Journal of Geophysical Research: Solid Earth* 105(B7):16,391–16,402, DOI 10.1029/2000JB900095
- Berardino P., Fornaro G., Lanari R., Sansosti E. (2002) A new algorithm for surface deformation monitoring based on small baseline differential SAR interferograms. *Geoscience and Remote Sensing, IEEE Transactions on* 40(11):2375–2383, DOI 10.1109/TGRS.2002.803792
- Biggs J., Wright T., Lu Z., Parsons B. (2007) Multi-interferogram method for measuring interseismic deformation: Denali Fault, Alaska. *Geophysical Journal International* 170(3):1165–1179, DOI 10.1111/j.1365-246X.2007.03415.x
- Biggs J., Lu Z., Fournier T., Freymueller J. T. (2010) Magma flux at Okmok Volcano, Alaska, from a joint inversion of continuous GPS, campaign GPS, and interferometric synthetic aperture radar. *Journal of Geophysical Research: Solid Earth* 115(B12), DOI 10.1029/2010JB007577
- Byrd H. R., Gilbert C. J., Nocedal J. (2000) A trust region method based on interior point techniques for nonlinear programming. *Mathematical Programming* 89(1):149–185, DOI 10.1007/PL00011391
- Casu F., Manzo M., Pepe A., Lanari R. (2008) SBAS-DInSAR analysis of very extended areas: First results on a 60,000- km² test site. *Geoscience and Remote Sensing Letters, IEEE* 5(3):438–442, DOI 10.1109/LGRS.2008.916199
- Deo N. (2004) *Graph theory with applications to engineering and computer science*. PHI Learning Pvt. Ltd., 478 pp.
- Emardson T. R., Simons M., Webb F. H. (2003) Neutral atmospheric delay in interferometric synthetic aperture radar applications: Statistical description and mitigation. *Journal of Geophysical Research: Solid Earth* 108(B5), DOI 10.1029/2002JB001781
- Feigl K. L. (2002) Measurement of coseismic deformation by satellite geodesy. In: Lee W. H. K., Kanamoori H., Jennings P. C. (eds) *International Handbook of Earthquake and Engineering Seismology*, vol 81A, Academic Press, pp 607–620
- Feigl K. L., Thurber C. H. (2009) A method for modelling radar interferograms without phase unwrapping: application to the M 5 Fawnskin, California earthquake of 1992 December 4. *Geophysical Journal International* 176(2):491–504, DOI 10.1111/j.1365-246X.2008.03881.x
- Feigl K. L., Sargent A., Jacq D. (1995) Estimation of an earthquake focal mechanism

- from a satellite radar interferogram: Application to the December 4, 1992 Landers aftershock. *Geophysical Research Letters* 22(9):1037–1040, DOI 10.1029/94GL03212
- Feigl K. L., Sarti F., Vadon H., McClusky S., Ergintav S., Durand P., Bürgmann R., Rigo A., Massonnet D., Reilinger R. (2002) Estimating slip distribution for the Izmit mainshock from coseismic GPS, ERS-1, RADARSAT, and SPOT measurements. *Bulletin of the Seismological Society of America* 92(1):138–160, DOI 10.1785/0120000830
- Feigl K. L., Le Mével H., Ali S. T., Córdova L., Andersen N. L., DeMets C., Singer B. S. (2014) Rapid uplift in Laguna del Maule volcanic field of the Andean Southern Volcanic zone (Chile) 2007–2012. *Geophysical Journal International* 196(2):885–901, DOI 10.1093/gji/ggt438
- Fialko Y., Sandwell D., Agnew D., Simons M., Shearer P., Minster B. (2002) Deformation on nearby faults induced by the 1999 Hector Mine earthquake. *Science* 297(5588):1858–1862, DOI 10.1126/science.1074671
- Fournier T. (2008) Analysis and Interpretation of Volcano Deformation in Alaska: Studies from Okmok and Mt. Veniamin Volcanoes. University of Alaska Fairbanks
- Fournier T., Freymueller J., Cervelli P. (2009) Tracking magma volume recovery at Okmok volcano using GPS and an unscented Kalman filter. *Journal of Geophysical Research: Solid Earth* 114(B2), DOI 10.1029/2008JB005837
- Freymueller J. T., Kaufman A. M. (2010) Changes in the magma system during the 2008 eruption of Okmok volcano, Alaska, based on GPS measurements. *Journal of Geophysical Research: Solid Earth* 115(B12), DOI 10.1029/2010JB007716
- Haney M. M. (2010) Location and mechanism of very long period tremor during the 2008 eruption of Okmok Volcano from interstation arrival times. *Journal of Geophysical Research: Solid Earth* 115(B10), DOI 10.1029/2010JB007440, b00B05
- Hanssen R. (2001) Radar Interferometry: Data Interpretation and Error Analysis. Remote Sensing and Digital Image Processing, Springer Netherlands, 308 pp., DOI 10.1007/0-306-47633-9
- Harris J. M., Hirst J. L., Mossinghoff M. J. (2008) Combinatorics and Graph Theory, vol 2. Springer, 381 pp.
- Hetland E., Musé P., Simons M., Lin Y., Agram P., DiCaprio C. (2012) Multiscale InSAR Time Series (MInTS) analysis of surface deformation. *Journal of Geophysical Research: Solid Earth* 117(B2), DOI 10.1029/2011JB008731
- Hetland E. A., Hager B. H. (2005) Postseismic and interseismic displacements near a strike-slip fault: A two-dimensional theory for general linear viscoelastic rheologies. *J. Geophys. Res. (Solid Earth)* 110:10,401
- Hooper A. (2008) A multi-temporal InSAR method incorporating both persistent scatterer and small baseline approaches. *Geophysical Research Letters* 35(16):L16,302, DOI 10.1029/2008GL034654, 116302
- Hooper A., Zebker H., Segall P., Kampes B. (2004) A new method for measuring deformation on volcanoes and other natural terrains using InSAR persistent scatterers. *Geophysical Research Letters* 31(23), DOI 10.1029/2004GL021737
- Jellinek A., DePaolo D. J. (2003) A model for the origin of large silicic magma chambers: precursors of caldera-forming eruptions. *Bulletin of Volcanology* 65(5):363–381, DOI

- 10.1007/s00445-003-0277-y
- Jolivet R., Simons M., Agram P. S., Duputel Z., Shen Z.-K. (2015) Aseismic slip and seismogenic coupling along the central San Andreas Fault. *Geophysical Research Letters* 42(2):297–306, DOI 10.1002/2014GL062222
- Lanari R., Casu F., Manzo M., Lundgren P. (2007) Application of the SBAS-DInSAR technique to fault creep: A case study of the Hayward fault, California. *Remote Sensing of Environment* 109(1):20–28, DOI 10.1016/j.rse.2006.12.003
- Le Mével H., Feigl K. L., Cordova L., DeMets C., Lundgren P. (2015a) Evolution of unrest at Laguna del Maule volcanic field (Chile) from InSAR and GPS measurements, 2003 to 2014. *Geophysical Research Letters* 42(16):6590–6598, DOI 10.1002/2015GL064665
- Le Mével H., Gregg P. M., Feigl K. L. (2015b) Magma injection models to quantify reservoir dynamics at Laguna del Maule volcanic field, Chile, between 2007 and 2015. In: 2015 Fall Meeting, American Geophysical Union, URL <https://agu.confex.com/agu/fm15/webprogram/Paper74502.html>
- Le Mével H., Gregg P., Feigl K. L. (2016) Magma injection into a long-lived reservoir to explain geodetically measured uplift: application to the 2007–2014 unrest episode at Laguna del Maule volcanic field, Chile. *Journal of Geophysical Research: Solid Earth* DOI 10.1002/2016JB013066, 2016JB013066
- Lee C.-W., Lu Z., Jung H.-S. (2012) Simulation of time-series surface deformation to validate a multi-interferogram InSAR processing technique. *International Journal of Remote Sensing* 33(22):7075–7087, DOI 10.1080/01431161.2012.700137
- Lu Z., Dzurisin D. (2014) InSAR imaging of Aleutian volcanoes. In: *InSAR Imaging of Aleutian Volcanoes*, Springer Praxis Books, Springer Berlin Heidelberg, pp 87–345, DOI 10.1007/978-3-642-00348-6
- Lu Z., Masterlark T., Dzurisin D. (2005) Interferometric synthetic aperture radar study of Okmok volcano, Alaska, 1992–2003: Magma supply dynamics and postemplacement lava flow deformation. *Journal of Geophysical Research: Solid Earth* 110(B2), DOI 10.1029/2004JB003148
- Lu Z., Dzurisin D., Biggs J., Wicks C., McNutt S. (2010) Ground surface deformation patterns, magma supply, and magma storage at Okmok volcano, Alaska, from InSAR analysis: 1. Interruption deformation, 1997–2008. *Journal of Geophysical Research: Solid Earth* 115(B5), DOI 10.1029/2009JB006969
- Massonnet D., Feigl K. L. (1995) Discrimination of geophysical phenomena in satellite radar interferograms. *Geophysical Research Letters* 22(12):1537–1540, DOI 10.1029/95GL00711
- Massonnet D., Feigl K. L. (1998) Radar interferometry and its application to changes in the Earth's surface. *Reviews of Geophysics* 36(4):441–500, DOI 10.1029/97RG03139
- Masterlark T., Haney M., Dickinson H., Fournier T., Searcy C. (2010) Rheologic and structural controls on the deformation of Okmok volcano, Alaska: FEMs, InSAR, and ambient noise tomography. *Journal of Geophysical Research: Solid Earth* 115(B2), DOI 10.1029/2009JB006324
- Masterlark T., Donovan T., Feigl K. L., Haney M., Thurber C. H., Tung S. (2016) Volcano deformation source parameters estimated from insar: Sensitivities to uncertainties in

- seismic tomography. *Journal of Geophysical Research: Solid Earth* pp URL %<http://dx.doi.org/10.1002/2015JB012656>, 2015JB012656
- MATLAB (2014) version 8.3.0.532 (R2014a). The MathWorks Inc., Natick, Massachusetts, URL <http://www.mathworks.com/products/matlab>
- Merris R. (1994) Laplacian matrices of graphs: a survey. *Linear Algebra and its Applications* 197–198(0):143–176, DOI [http://dx.doi.org/10.1016/0024-3795\(94\)90486-3](http://dx.doi.org/10.1016/0024-3795(94)90486-3)
- Mogi K. (1958) Relations between the eruptions of various volcanoes and the deformations of the ground surfaces around them. *Bulletin of the Earthquake Research Institute* 36:99–134
- Ohlendorf S. (2015) Investigation of volcanic processes using seismology and geodesy at Okmok Volcano, Alaska. Madison, Wis.: University of Wisconsin–Madison, 2015.
- Ohlendorf S. J., Thurber C. H., Pesicek J. D., Prejean S. G. (2014) Seismicity and seismic structure at Okmok Volcano, Alaska. *Journal of Volcanology and Geothermal Research* 278–279(0):103–119, DOI 10.1016/j.jvolgeores.2014.04.002
- Perissin D., Wang T. (2012) Repeat-pass SAR interferometry with partially coherent targets. *Geoscience and Remote Sensing, IEEE Transactions on* 50(1):271–280, DOI 10.1109/TGRS.2011.2160644
- Prescott W. H. (1976) An extension of Frank’s method for obtaining crustal shear strains from survey data. *Bulletin of the Seismological Society of America* 66(6):1847–1853
- Schmidt D. A., Bürgmann R. (2003) Time-dependent land uplift and subsidence in the Santa Clara valley, California, from a large interferometric synthetic aperture radar data set. *Journal of Geophysical Research: Solid Earth* 108(B9), DOI 10.1029/2002JB002267
- Schmidt R. (1996) Least squares range difference location. *Aerospace and Electronic Systems, IEEE Transactions on* 32(1):234–242, DOI 10.1109/7.481265
- Segall P. (2010) *Earthquake and Volcano Deformation*. Princeton University Press, 456 pp.
- Spielman D. A. (2010) Algorithms, graph theory, and linear equations in laplacian matrices. In: *Proceedings of the International Congress of Mathematicians*, vol 4, pp 2698–2722, DOI 10.1.1.165.8870
- Strang G., Borre K. (1997) *Linear Algebra, Geodesy, and GPS*. Siam, 624 pp.
- Wackerly D., Mendenhall W., Scheaffer R. (2007) *Mathematical Statistics with Applications*. Cengage Learning, 944 pp.
- Zebker H. A., Goldstein R. M. (1986) Topographic mapping from interferometric synthetic aperture radar observations. *Journal of Geophysical Research: Solid Earth* 91(B5):4993–4999, DOI 10.1029/JB091iB05p04993